Synthesis and Structure-Property Relationships of Polyimide Covalent Organic Frameworks for Carbon Dioxide Capture and (Aqueous) Sodium-Ion Batteries

Van Der Jagt, Remco; Vasileiadis, Alexandros; Veldhuizen, Hugo; Ganapathy, Swapna; Habisreutinger, Nicolas C.; Van Der Veen, Monique A.; Wang, Chao; Wagemaker, Marnix; Van Der Zwaag, Sybrand; Nagai, Atsushi

DOI
10.1021/acs.chemmater.0c03218

Publication date
2021

Document Version
Final published version

Published in
Chemistry of Materials

CHEMISTRY OF MATERIALS

pubs.acs.org/cm

Article

Synthesis and Structure–Property Relationships of Polyimide Covalent Organic Frameworks for Carbon Dioxide Capture and (Aqueous) Sodium-Ion Batteries

Remco van der Jagt,[⊥] Alexandros Vasileiadis,[⊥] Hugo Veldhuizen,[⊥] Pengpeng Shao, Xiao Feng, Swapna Ganapathy, Nicolas C. Habisreutinger, Monique A. van der Veen, Chao Wang, Marnix Wagemaker,* Sybrand van der Zwaag, and Atsushi Nagai*

Cite This: *Chem. Mater.* 2021, 33, 818–833

Read Online

ACCESS | Metrics & More | Article Recommendations | Supporting Information

ABSTRACT: Covalent organic frameworks (COFs) are an emerging material family having several potential applications. Their porous framework and redox-active centers enable gas/ion adsorption, allowing them to function as safe, cheap, and tunable electrode materials in next-generation batteries, as well as CO_2 adsorption materials for carbon-capture applications. Herein, we develop four polyimide COFs by combining aromatic triamines with aromatic dianhydrides and provide detailed structural and electrochemical characterization. Through density functional theory (DFT) calculations and powder X-ray diffraction, we achieve a detailed structural characterization, where DFT calculations reveal that the imide bonds prefer to form at an angle with one another, breaking the 2D symmetry, which shrinks the pore width and elongates the pore walls. The eclipsed perpendicular stacking is preferable, while sliding of the COF sheets is energetically accessible in a relatively flat energy landscape with a few metastable regions. We investigate the potential use of these COFs in CO_2 adsorption and electrochemical applications. The adsorption and electrochemical properties are related to the structural and chemical characteristics of each COF, giving new insights for advanced material designs. For CO_2 adsorption specifically, the two best performing COFs originated from the same triamine building block, which—in combination with force-field calculations—revealed unexpected structure–property relationships. Specific geometries provide a useful framework for Na-ion intercalation with retainable capacities and stable cycle life at a relatively high working potential (>1.5 V *vs* Na/Na^+). Although this capacity is low compared to conventional inorganic Li-ion materials, we show as a proof of principle that these COFs are especially promising for sustainable, safe, and stable Na-aqueous batteries due to the combination of their working potentials and their insoluble nature in water.

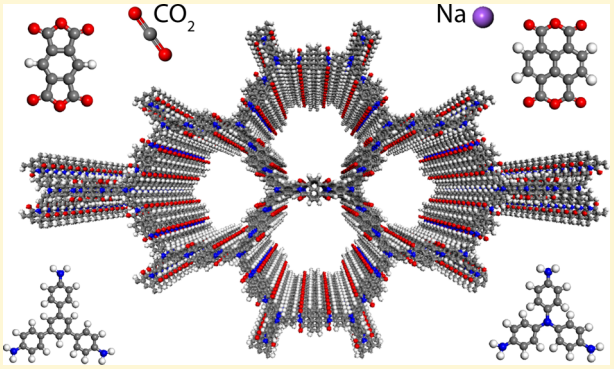

1. INTRODUCTION

Modern society is challenged by the necessity of a rapid energy transition toward renewable energy and electric transport while facing the continuous increasing effects of greenhouse gases. The usage of renewable sources, primarily based on solar and wind, is highly intermittent[1−8] and demands daily electrical energy storage for which stationary batteries appear to be a promising technology. Furthermore, the increasing importance of mobile technologies calls for new cheap and sustainable approaches, which motivates the search for organic electrode materials.[9−15] Also, limiting the carbon dioxide (CO_2) concentration in air is currently one of the key issues on the climate control agenda. In this framework, novel material investigations for electrochemical storage and CO_2-capture applications are performed toward a sustainable future.

Currently, Li-ion batteries are the most widely employed technology for reversible electrochemical energy storage systems[1] having the highest energy density, in particular suitable for mobile applications. Lately, Na-ion batteries are suggested to cooperate and even compete with Li-ion batteries in the energy transition due to the greater abundance of Na, albeit at the cost of a lower energy density.[10] In particular, aqueous batteries are considered to be promising for stationary storage,[11] based on their intrinsically lower costs and higher

Received: August 6, 2020
Revised: January 6, 2021
Published: January 21, 2021

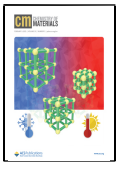

safety. Typical electrodes in batteries are based on transition metals (providing the redox center) for which mining and syntheses are energy-consuming and costly, motivating the search for organic alternatives. In 50 years, the world of organic electrodes has grown and contains now small organic compounds,[3,5] conductive polymers,[12] polycarbonyls,[6,13] polyradicals,[7] and more.[14,15] These can be designed to fit multiple applications and can be used for a diversity of batteries such as Li-ion, Na-ion, dual-ion, and multivalent-ion batteries. However, organic electrodes have (still) many drawbacks such as (a) poor stability and durability due to easy dissolution of small redox-active molecules in the electrolyte, (b) low energy efficiency due to the poor diffusion of ions through the electrode, and (c) a low electronic conductivity, demanding the addition of a large weight fraction of an electronic conducting agent, reducing the amount of active materials and thus the specific capacity of the electrode. As a result, the synthesis of two- or three-dimensional porous conductive polymers can be considered an important strategy. However, the complexity of designing such structures, while maintaining a low price and a sustainable process for the device, is a great challenge.

Covalent organic frameworks (COFs) are a class of two- or three-dimensional crystalline porous polymers composed of lightweight molecules linked by covalent bonds.[16−39] The periodicity of the structure results in a predictable porous polymer where the two-dimensional polymeric sheets stack on top of each other in the aim to create one-dimensional channels. Usually, the building blocks are linked by boroxines,[16] boronate esters,[23] imines,[40] triazines,[41] hydrazones,[42] azines,[43] or squaraines.[44] The development of new linkages to synthesize such covalent frameworks is essential to exploit the technological potential of this emerging class of materials. Polyimides are known for their high thermal stability[45−48] and excellent chemical resistance and are widely used as thermoplastics as well as in the electronic industry. In addition, polyimides can facilitate redox reactions,[13] making these promising electrode materials in batteries. Recently, imide-based COFs were reported,[45,47,48] introducing a new material family with high porosity, stability, and high availability from biomass. These properties may provide opportunities that answer the typical drawbacks of state-of-the-art organic electrodes and thus potentially may lead to the development of new redox-active polymers for cheap transition metal-free next-generation batteries. Several COFs have shown very promising electrochemical performances by obtaining high capacities and reliable cycling for Li-ion batteries.[49−53] Na-ion chemistries are also explored in the context of cheaper chemistry for large scale storage applications.[54−56]

COFs are additionally expected to play a central role in the sequestration of CO_2 from the atmosphere.[57] Carbon capture has become a well-known term over the last decades to indicate the need for efficient storage solutions of carbon-based greenhouse gases. In this context, nanoporous materials with well-defined pores are attracting increasing attention since their porous nature allows the efficient adsorption of gases, such as carbon dioxide.[58] Among such materials, COFs present a unique advantage by combining strong covalent bonds with a crystalline, porous architecture.[57] Their crystallinity facilitates directed research toward improved gas adsorption because of the precise control over pore sizes and shapes. In addition, the concept of pore structure engineering has been utilized to systematically investigate the effect of chemically or physically different pores on gas adsorption properties.[25,59] Although this concept has been extensively studied for boronate ester and imine-based COFs, such studies for more stable, high-performance COFs are scarce.[60,61] However, in order to utilize nanoporous adsorbents in industry applications, a thermally and chemically stable polymer backbone is often required. As such, polyimide-based COFs are expected to be promising candidates,[45,47,48] and systematically studying their gas sorption properties pushes the field forward.

In this work, we report the development of four mesoporous, redox-active polyimide COFs. One of the leading experimental challenges in the chemistry of the COFs for achieving complete structural characterization is crystallinity. Solving and refining crystal structures with atomic precision require the growth of single crystals, which has been scarcely reported.[62] For this reason, structure simulations are performed based on density functional theory (DFT), which brings forward an accurate description of their structural characteristics consistent with X-ray diffraction (XRD) measurements, shedding light on atomistic configurational preferences and providing insights for functional COFs. The developed COFs are evaluated as CO_2 sequestering and electrode materials by exploring their CO_2 adsorption and electrochemical properties. The operating redox potentials of the presented polyimide-based COFs and their insolubility in water make them suitable anode materials for aqueous batteries. Hence, we open up a new research direction for COFs by demonstrating the proof of principle of the (sodium) aqueous battery concept.

2. RESULTS AND DISCUSSION

2.1. COF Synthesis and Characterization. The polyimide COFs presented in this research were prepared by the imidization of aromatic triamines: tris(4-aminophenyl)amine (TAPA) or 1,3,5-tris(4-aminophenyl)benzene (TAPB) with aromatic dianhydrides: pyromellitic dianhydride (PMDA) or 1,4,5,8-naphthalenetetracarboxylic dianhydride (NTCDA). These four building blocks are commercially available. The solvothermal synthesis approach was applied for the imidization reactions using a solvent mixture of *N*-methyl-2-pyrrolidone (NMP) and *meta*-cresol and isoquinoline as the catalyst (detailed synthesis in the Supporting Information). The four different combinations of monomers allowed the formation of a set of four different polyimide polymers that are chemically relatively similar (Figure 1), but differ, for example, in pore size. Furthermore, the two aromatic dianhydride molecules (PMDA, NTCDA) can serve as redox-active sites for the reversible interaction with Li- and Na-ions, as will be discussed in the electrochemical characterization.

Fourier transformed infrared (FT-IR) confirmed the formation of polyimides by the presence of three primary specific imide vibrations (Figures S3−S6). First, we observed vibrational signals for the asymmetric and symmetric vibrations of the imide carbonyl C═O at 1720 and 1775 cm^{-1} for PIA, 1726, and 1778 cm^{-1} for PIB, 1674 and 1715 cm^{-1} for PIC, and 1672 and 1716 cm^{-1} for PID. The third absorption confirmed the presence of C−N−C stretching vibration at 1356 cm^{-1} for PIA, 1375 cm^{-1} for PIB, 1340 cm^{-1} for PIC, and 1344 cm^{-1} for PID. Final confirmation of the synthesis was supported by the disappearance of the characteristic starting material vibrations (around 3340 cm^{-1} for the amines and around 1765 cm^{-1} for the anhydride carbonyls). Additionally, solid-state nuclear magnetic resonance (NMR) measurements

https://dx.doi.org/10.1021/acs.chemmater.0c03218
Chem. Mater. 2021, 33, 818−833

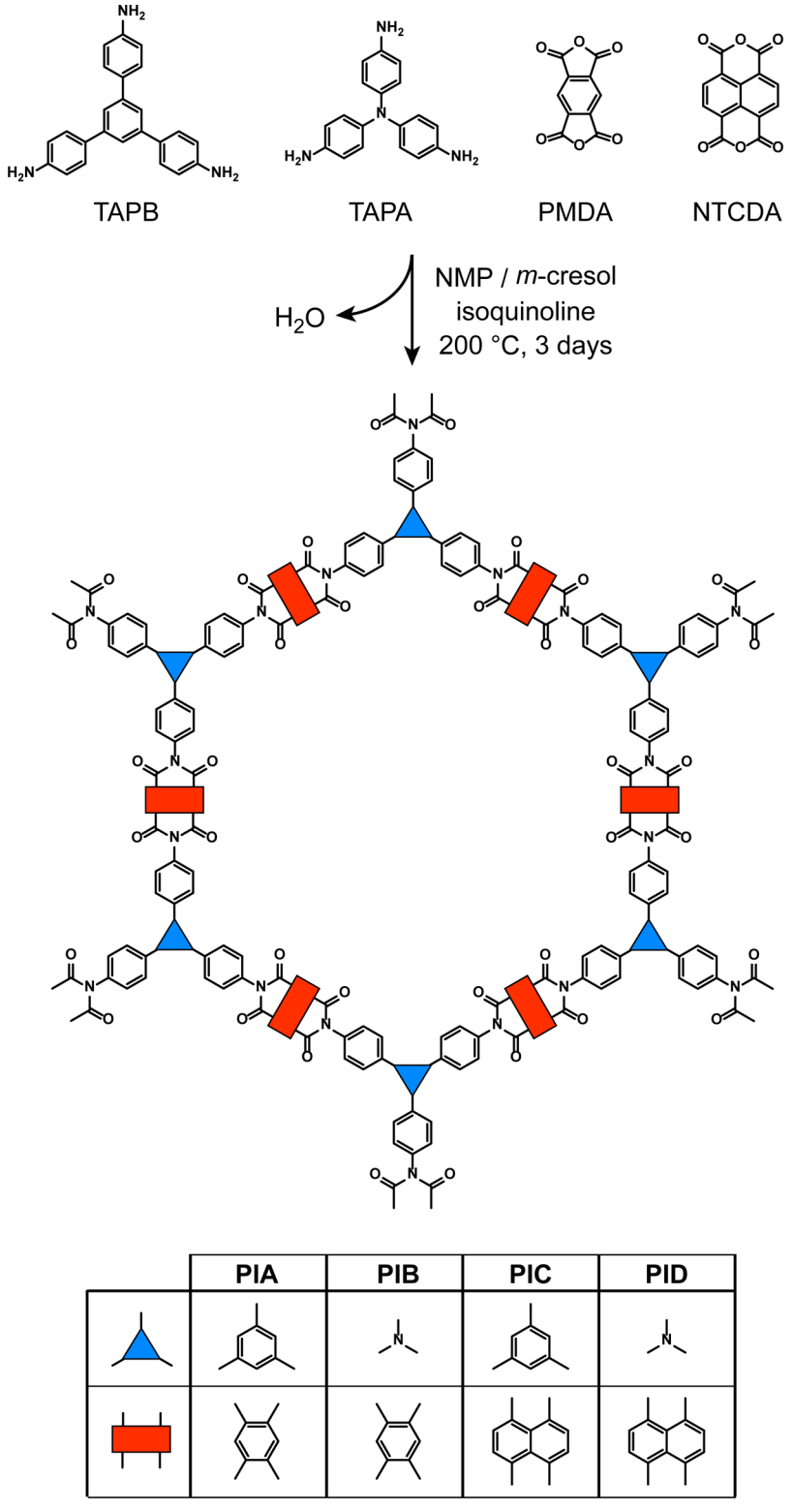

Figure 1. Synthesis scheme and the tags of the four polyimide COFs prepared from TAPB, TAPA, PMDA, and NTCDA.

were performed on the four COFs (Figures S7−S12). The precursors TAPA (linker of PIB and PID) and NTCDA (the active part of PIC and PID) are not traceable in the NMR spectra of PIA−PID, confirming the successful synthesis.

Polyimides are well known to be thermally and chemically stable polymers, which is apparent from their usage in high-performance applications. Here, we demonstrated that similar stability is retained when imides are employed as the connecting linkages in COFs. The four PI−COFs show high thermal stability as determined by thermogravimetric analysis (TGA): up to 535 °C for PIA and PIC, 525 °C for PIB, and 520 °C for PID (Figures S13−S16). In addition, the chemical stability was investigated by storing PIC and PID for 14 days in organic [1 M $NaClO_4$ in ethylene carbonate (EC)/dimethyl

https://dx.doi.org/10.1021/acs.chemmater.0c03218
Chem. Mater. 2021, 33, 818−833

carbonate (DMC)] and aqueous electrolyte (1 M Na_2SO_4 in neutral water), after which newly measured powder XRD (PXRD) spectra of the COFs were compared to the spectra of the as-synthesized materials (Figure S17). No significant changes were observed while comparing the spectra: even the secondary crystalline peaks are retained after these tests, reinforcing the suggested chemical stability of polyimide COFs.

The morphologies of the herein prepared COFs were determined *via* scanning electron microscopy (SEM) (Figure S18). In general, the microstructures of these polymers resemble large (radii of >1 μm) semi-spherical particles, which are highly aggregated. Furthermore, a zoom-in of such a particle revealed a sponge-like morphology with macropores in the order of 100 nm. To investigate the micro and mesopores, however, nitrogen gas sorption measurements provided a more quantitative insight for the porous structures of the four COFs.

The curves of the nitrogen sorption isotherms (at 77 K) of the four porous polymers (Figures S19–S22) all show a steep increase in N_2 uptake in the low relative pressure region (P/P_0 < 0.2). This behavior typically indicates the presence of both micropores and small mesopores. Interestingly, there seems to be a distinction between PMDA-derived polymers (PIA and PIB) and NDA-derived polymers (PIC and PID), where the latter polymers display a significant shoulder in their nitrogen isotherms. This observation indicates that the presence of mesopores is more pronounced in PIC and PID than in PIA and PIB. To verify this conclusion, the isotherms were fitted to a quenched-solid DFT model to calculate pore size distributions (PSDs, Figure S23). These PSDs indeed reveal the presence of a large number of micropores with respect to the expected mesopores, which is most notable for PIA and PIB. While PXRD results later indicate distinct repeating pore sizes for all four polymers, it is essential to realize that these gas sorption experiments reveal broad distributions of pore sizes originating from both crystalline and amorphous segments. Finally, the Brunauer–Emmett–Teller (BET) theory was applied to the nitrogen isotherms to calculate the BET surface area. Coincidentally, the BET surface area values for the polymers were in ascending order: 580 $m^2\ g^{-1}$ for PIA, 760 $m^2\ g^{-1}$ for PIB, 990 $m^2\ g^{-1}$ for PIC, and 1430 $m^2\ g^{-1}$ for PID (Figures S24–S27).

2.2. DFT Simulations for Accurate Material Characterization. In order to elucidate the structural characteristics of the COF structures, DFT calculations were performed. The quantum-mechanical treatment of the DFT method can predict configurational preferences more accurately as compared to classical force field approaches.[29] A detailed description of the computations is given in the Experimental Section.

Models for the PIA and PIB structures have been previously reported in the literature where several unit cell descriptions, optimized with the universal force field, were considered, namely, the AA eclipsed ($P6_3/mmm$), the serrated ($Cmcm$) where adjacent sheets are slipped by 1/4 of the unit cell distance, and the AB staggered ($P6_3/mmc$) stackings.[45] Both the eclipsed and serrated simulated PXRD patterns matched the experimental data. However, the serrated description was considered more probable based on the high gas uptake observed.[45] The PID structure has been recently reported to acquire a 2D hexagonal layered configuration based on TEM imaging.[47] The packing on the perpendicular direction remains uncertain due to the broadness of the PXRD peaks; however, the eclipsed AA stacking was put forward as it compared well with simulated PXRD patterns.[47]

Herein, we perform structural optimizations of a variety of possible hexagonal unit cell configurations. Our investigation also includes possibilities regarding intra-molecular configurations, such as the presence of torsion between the components of the COFs. The simulations reveal that it is energetically favorable for the benzene rings of both the TAPA and TAPB linkage molecules to break the 2D symmetry by exhibiting torsion, tilting to form equal angles with one another. The preferable torsion is demonstrated in Figure 2,

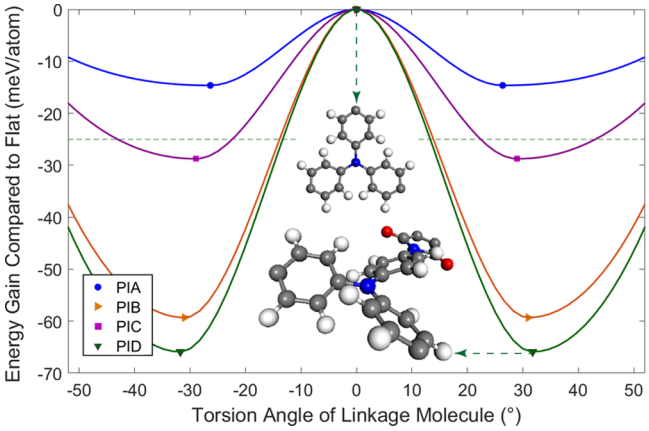

Figure 2. Energy gain as a function of the torsion angle between the benzene rings of the linkage molecules. All calculations per COF, initialized with an initial torsion of 10, 20, 30, 40, and 50°, relaxed toward the same configuration.

where the energy landscape as a function of the torsion angle in the linkage molecules is presented. Simulations with initial torsion angles between the carbon rings of the linkage molecules of 10, 20, 30, 40, and 50° were performed for the four COFs. Irrespectively of the initial angle, during geometry optimization, all the structures relaxed toward a preferable angle (minimum energy points in Figure 2), which is characteristic for each COF. This indicates that there is no barrier present for this transformation. When initializing the simulations in the perfectly 2D eclipsed configuration, all structures retained zero torsion angle configurations obtaining, however, much higher energies. Thus, the flat 2D configuration, which has dominantly brought forward as the best description in the literature, appears to be unstable (or marginally metastable) and is expected to transform naturally to a non-flat configuration exhibiting torsion. Macroscopically, the sheets will still appear as 2D structures due to the large size of the ab-plane. The observed trends in Figure 2 reveal that the torsion is much more stable for the COFs acquiring the TAPA linkage molecule (PIB and PID). The above observation seems reasonable as the single N atom in the center allows more rotational freedom than the center benzene ring of the TAPB linkage. This is also reflected in the slightly higher torsion angles of the TAPA linkage-containing configurations PIB and PID. A weaker effect is caused by the presence of the active molecule, with the NTCDA being more stable when combined with the tilted linkages than the PMDA. The torsion angle between the active molecules and the adjacent benzene ring of the linkages stabilized in all calculations at 25° for PIA, 36° for PIB, 56° for PIC, and 47° for PID.

https://dx.doi.org/10.1021/acs.chemmater.0c03218
Chem. Mater. 2021, 33, 818–833

These structural aspects have a significant impact on the lattice of the COF structures. Torsion in the linkage molecules shrinks and elongates the ab-plane and *c* lattice parameter, respectively, when compared to the flat structure (Figure 3a).

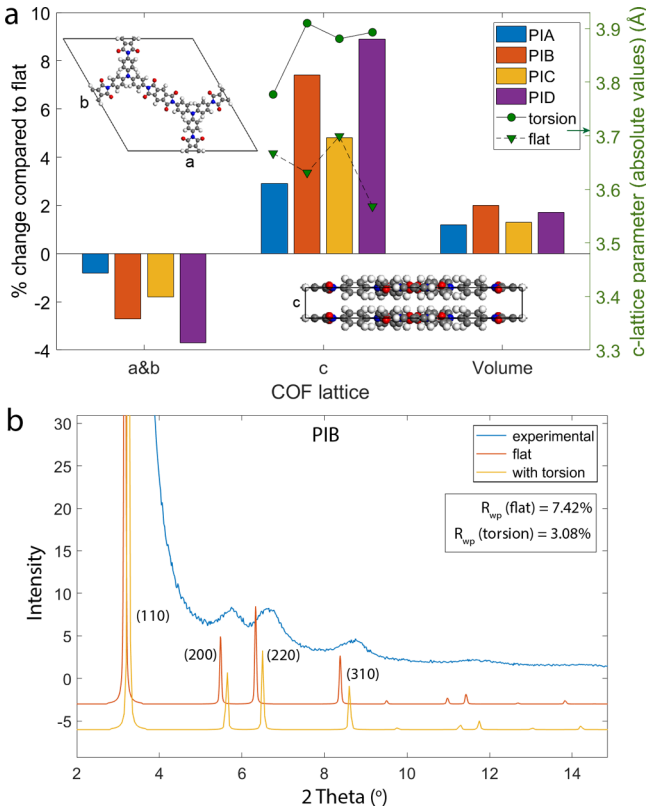

Figure 3. (a) Comparison between the flat and tilted COF configurations. The absolute values of the obtained *c*-lattice parameters are also provided (green scatter plot, right axis). (b) Effect of the presence of torsion in the crystal lattice of PIB on the PXRD simulated reflections, in comparison with the experimental pattern. Pawley refinement with the flat symmetry resulted in poorer agreement factors consistent with the torsion predicted by the DFT simulations.

A larger torsion angle in the linkages for the PIB and PID dictates greater elongation of the *c* lattice parameter and allows a more compact packing in the ab-plane, explaining why the TAPA-containing COF structures are affected the strongest. In absolute values, the PIB and PID structures obtain larger *c* lattice parameters (Figure 3a). The PMDA active molecule is rather small so that its rotation does not have an impact on the lattice (PIA and PIB), but the larger NTCDA molecule that tilted 56° in PIC does contribute.

The structural characteristics mentioned above are expected to have an impact on the properties of the COF structures. Torsion provides longer pore-walls since the *c* lattice parameter runs along the channels of the porous structure, enabling more space for gas molecules or charge carrier ions to be attached, as the same pore depth can be achieved with fewer stacks. Elongation of the pore walls due to torsion is likely to have an additional effect, enabling gas molecules and charge carrier ions to access from the outside, which creates an otherwise inaccessible pore due to morphological aspects (such as miss-orientation of one COF ring blocking the pathway). However, validating this proposition requires further calculations outside the scope of this study.

The next step is to investigate the packing in the perpendicular direction. For COFs, there are two extreme options, namely, the AA eclipsed, where adjacent sheets fall precisely on top of each other, and the AB staggered stacking, where adjacent sheets are slipped by 1 unit cell. In between, there is a wide variety of serrated configurations where adjacent sheets are slipped, creating an offset (Figure 4a). The relative stability of the AA eclipsed and AB staggered stacking for the 4 COFs was evaluated. The AA eclipsed stacking was the most stable configuration in all COFs and is set as the 0 energy reference. Recently, a DFT study revealed that 2D layered COFs based on 2,3,6,7,10,11-hexahydroxytriphenylene and 4,4′-diphenyl-1-butadiynebis have a strong preference for slight offsets in the range of 1.7 Å rather than a true eclipsed AA structure.[29] Herein, we investigate if there is a similar trend in the polyimide COFs, calculating configurations with a variety of offsets for the PIA and PID (Figure 4b,c). The truly eclipsed AA stacking remains the most stable configuration in both cases. The PID configuration with an offset of 1.5 Å even relaxed back during the simulation to the eclipsed configuration.

The energy landscape, however, does not monotonously increase as we move away from the eclipsed configuration, as a metastable serrated-stacking region is found with a local minimum where the sheets are slipped 6.6 Å (~1/3 of the distance between the AA and AB stacking, Figure 4d). The small energy penalty for offsets indicates that the metastable phase might be stabilized but is likely to fall back toward the eclipsed configuration under thermal energy and stresses caused, for example, by Li or Na insertion. For large offsets, where adjacent sheets are slipped more than 1/2 the unit cell distance, the energy penalty rises to reach the unstable AB configuration in both PIA and PID. This is best demonstrated for the PIA, where the energy landscape is monotonously increasing as the sheets move away from the eclipsed configuration, reaching the unstable AB staggered configuration. The PIA energy map (Figure 4c) also suggests that the offsets are more likely to occur in the direction toward the AB staggered stacking (*i.e.*, represented by the corners of the hexagonal energy maps). The energy difference in favor of the AA stacking is likely to originate from the greater molecular overlap leading to more significant van der Waals attraction forces. The above is in agreement with the eclipsed stacking put forward for PID based on TEM and PXRD experiments.[47] Based on the measured BET surface, PIA and PIB were previously reported in serrated configurations.[45] This seems, however, not a strong argument since the measured surfaces are dominated by morphological features rather than the crystal lattice. Our simulations indicate that the relatively flat energy landscape, especially for small offsets, might allow the sheets to slide on one another temporarily; however, the thermodynamically favorable phase is the eclipsed AA stacking. Due to computational cost, energy maps for the PIB and PIC were not constructed. Nevertheless, it is likely that they follow similar behavior. Interestingly, according to Figure 4a, the ab-staggered configuration of these structures has a much smaller energy penalty.

Measured PXRD patterns of the 4 COFs were subjected to Pawley refinement based on the optimized DFT structures (hexagonal eclipsed AA stacking, presence of torsion), resulting in good agreement, as shown in Figure 5. The

https://dx.doi.org/10.1021/acs.chemmater.0c03218
Chem. Mater. 2021, 33, 818−833

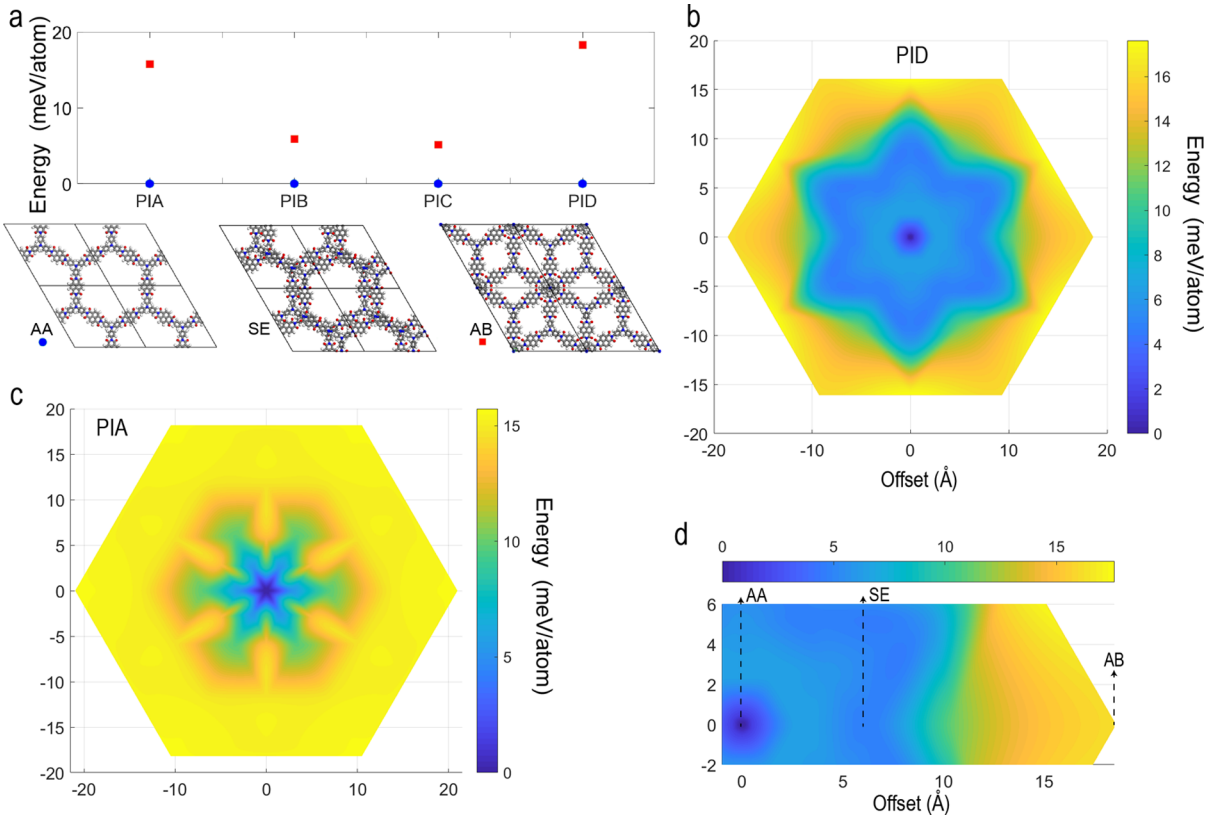

Figure 4. (a) Energy difference between the AA eclipsed, AB staggered stacking for the 4 COFs, an illustration of the AA eclipsed, AB staggered and an example of serrated stacking (SE), (b) energy landscape of PID, (c) energy landscape of PIA, and (d) zoom-in in the energy landscape of PID along the direction toward the AB stacking where the metastable SE at an offset of 6.6 Å is visible. Note that the orientation of the unit cell illustration in (a) is not the same as the orientation of the energy maps. In the energy maps, the corners of the hexagons represent the AB staggered configuration.

predicted torsion breaks the 2D symmetry in the $P6_3/mmm$ space group, resulting in unit cells that can be described by the $C222$ (21) or $C222_1$ (20) symmetries and in the hexagonal unit cell by the $P622$ (177) or $P\bar{3}1m$ (162) symmetries. Crystallographic data for the 4 COF structures in a variety of unit cell descriptions can be found in the Supporting Information. The simulated PXRD data of the eclipsed AA stacking match well with the experimental reflections, consistent with the DFT results presented above, that predict the AA stacking to be the most stable configuration. The obtained lattice parameters in the hexagonal description were $a = b = 36.38$ Å and $c = 3.79$ Å for the PIA ($P\bar{3}1m$), $a = b = 31.37$ Å and $c = 3.91$ Å for the PIB ($P622$), $a = b = 37.07$ Å and $c = 3.89$ Å for the PIC ($P\bar{3}1m$), and $a = b = 31.94$ Å and $c = 3.90$ Å for the PID ($P622$). The calculated pore sizes presented in Figure 5 match exceptionally well with the ones determined with XRD.

The c-lattice parameter quantifies the distance between the sheets in these COF structures. The model found in the literature for the polyimide PID−COF predicted a c-lattice parameter of 4.37 Å.[47] The DFT calculations, based on the DFT-DF3 method of Grimme to account for the van der Waals forces (see Experimental Section), reveal that the c-lattice parameter is significantly smaller amounting 3.90 Å, similar to the distance predicted for PIB at 3.91 Å. The sensitivity of our result on the choice of the DFT method is investigated by performing calculations on the PIB structure implementing a variety of van der Waals corrections on the PBE functional as well as the vdW-DF functionals of Langreth and Lundqvist *et al.*,[63,64] the results of which are presented in Figure S28. Without the van der Waals corrections (PBE method), we obtain a c-lattice parameter of 4.45 Å, a 14% overestimation of the c-lattice parameter (12% in volume), an error with the same magnitude as commonly observed in the literature.[65] By including van der Waals interactions, however, the c-lattice parameter is predicted to be on average (all methods) 3.88 ± 0.11 Å, larger than the 3.43 Å presented in a previous study assuming a perfectly flat structure.[45] Due to the lack and/or broadness of the PXRD reflections from these materials, it is possible to obtain acceptable agreement factors with the use of Pawley refinement for a wide range of lattice parameters. Consistent with our description that includes torsion, Pawley refinement based on the perfectly flat hexagonal unit cell ($P6_3/mmm$) resulted in worse agreement factors than when refined with the proposed configurations, including torsion. A more valid check is the comparison of the predicted reflections of the two cases (presence torsion and flat). This is a tough task considering the quality of the reflections; however, it was possible to isolate this behavior in the PIB PXRD pattern. In Figure 3b, we observe that the presence of torsion shifts the ab-plane reflections to higher angles. The above observation is a clear indication of the plane-shrinkage due to torsion, leading to significantly better agreement with the experimental XRD results. In addition, a different approach was attempted by performing simulations on the flat, SE, unit cell ($Cmcm$) for the PIB COF reported in the literature.[45] The offset created the conditions to break the 2D symmetry during relaxation, and the structure relaxed to

https://dx.doi.org/10.1021/acs.chemmater.0c03218
Chem. Mater. 2021, 33, 818−833

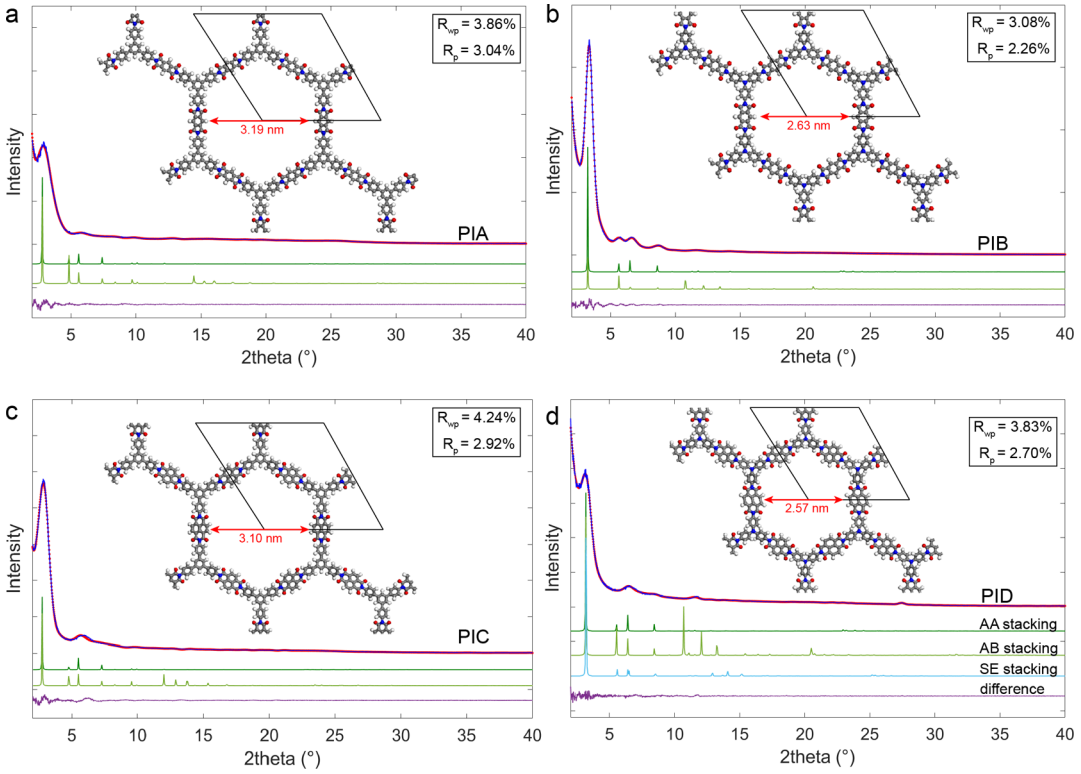

Figure 5. Experimental (blue line) *vs* Pawley refined (red scatter) *vs* simulated (dark green line for AA and light green line for the AB stacking) PXRD data for the (a) PIA, (b) PIB, (c) PIC, and (d) PID COFs.

exhibit torsion (~32°) in the linkage molecules ($C222_1$ symmetry) consistent with the hexagonal description. When sliding the sheets to an eclipsed configuration, we obtained lower energies, in agreement with the results obtained for the hexagonal unit cell. These new insights, the role of torsion in the COF structures, are crucial to understand and tailor the functional properties of these materials.

2.3. CO_2 Adsorption Properties. The porosity of the four polyimide COFs was further analyzed by CO_2 gas sorption. The efficient storage of greenhouse gases such as CO_2 in COFs has gained increasing attention in recent years because their pore sizes approach the physical size of the gasses (allowing high uptake) and have even shown to be selective when exposed to gas mixtures.[57] Polyimides are particularly interesting since their high thermal and chemical stability make them attractive surfaces for CO_2 capture under industrially realistic conditions.

Figure 6a shows the CO_2 adsorption isotherms of PIA, PIB, PIC, and PID from 0.02 to 1.2 bar at 273 K. Generally, the best CO_2 adsorbents in terms of storage capacity are the ones that contain mostly micropores.[57] Despite the fact that the four COFs discussed here contain a significant amount of mesopores, their CO_2 capacities (at 1 bar) are relatively high: 51 $cm^3\ g^{-1}$ for PIA, 64 for PIB, 56 for PIC, and 66 for PID. While these capacity values allowed us to benchmark the performance of the four new systems against other COFs, the shape of the CO_2 isotherms revealed additional information about the porous architecture. Similar to the results for N_2 sorption, PIA and PIB have a significantly different CO_2 adsorption behavior than PIC and PID. The slope in the low-pressure (<0.2 bar) region is for all polymers higher than that in the higher-pressure (>0.6 bar) region, but the curves of PIA and PIB tail off more rapidly than those of PIC and PID. This behavior is directly correlated with the difference in PSD (Figure S23) described earlier. Furthermore, Figure 6b shows the CO_2 capacities (1 bar, 273 K) and BET surface areas of the four polyimide COFs. These two material properties do not seem to be completely correlated with each other for all polymers, which emphasizes again that the pore size effect seems to be the dominant but not the sole feature responsible for the observed CO_2 capacities.

To gain further insights into the sorption of CO_2 molecules into the COF host structures, we performed force-field calculations. Results are presented in Figure 6c for the adsorption of CO_2 at 273 K and pressure of 1 bar. We observe that adsorption in the inner pore surface of PIA forms a hexagonal CO_2 density with relatively homogeneous binding energies. However, for PIB and PID, we observe that the density distribution resembles more of a star-like dissipation, where the more significant rotation of the TAPA molecule results in the formation of favorable potential wells (blue areas of the distribution). Interestingly, we have previously observed similar CO_2 capacity differences for other TAPB-/TAPA-based COFs,[48] which suggests that the TAPA linkage segments may play a bigger role than originally expected. For all COFs, we observe that adsorption is more favorable near the linkage molecules where the amount of hydrogen exposed to the oxygen atoms of the CO_2 is higher.

The CO_2 adsorption study presented here shows that small molecular changes in the framework of polyimide-based COFs lead to significantly different CO_2 capacities. A review about the effect of COF pore sizes on their CO_2 capacity has been presented by Zeng *et al.*,[57] and we adapted its key figure by adding the results of the polyimide-based COFs described here (Figure 7). Only PIC and PID were added for this comparison since their PSDs calculated from N_2 adsorption showed the

https://dx.doi.org/10.1021/acs.chemmater.0c03218
Chem. Mater. 2021, 33, 818−833

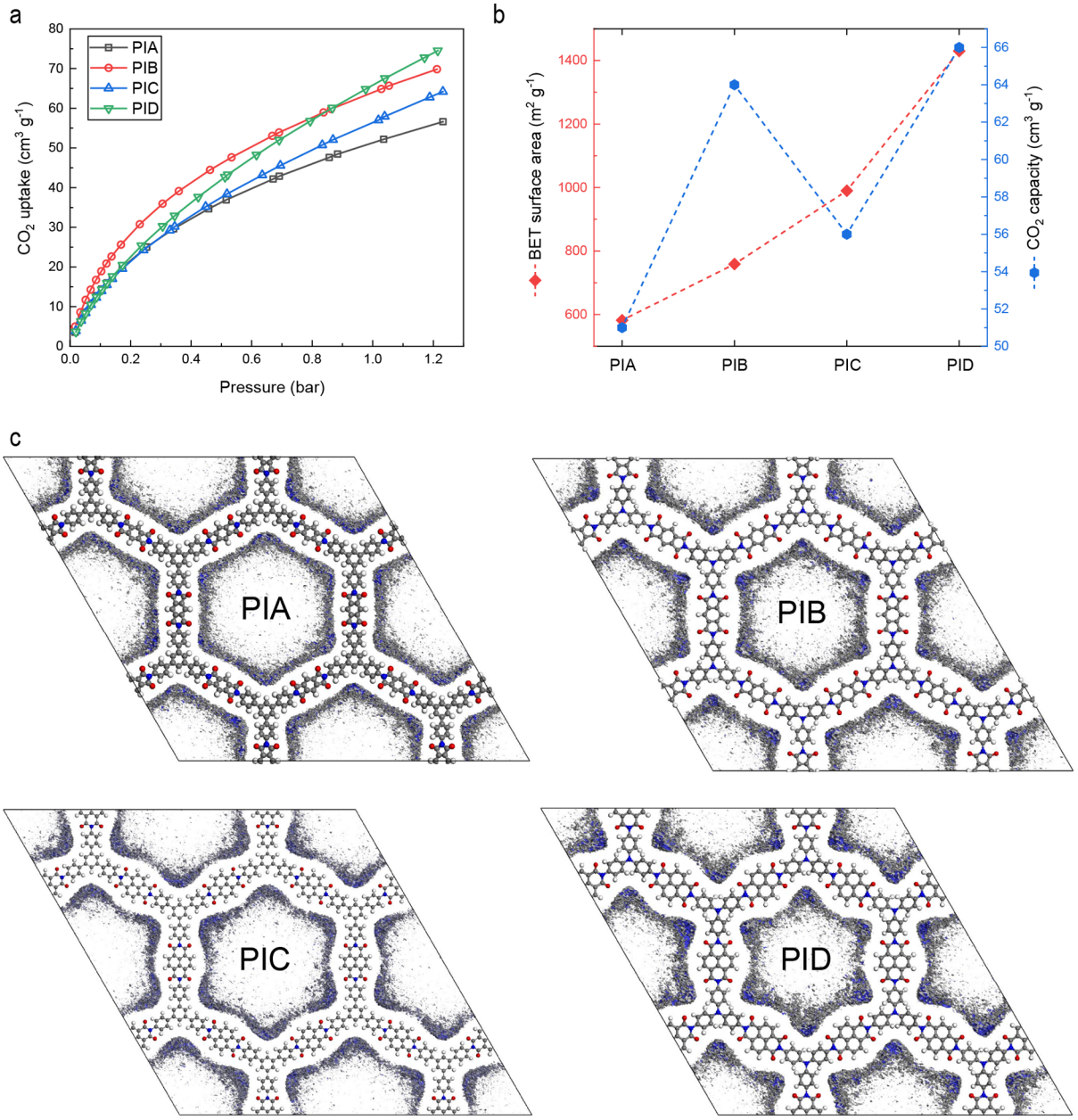

Figure 6. (a) Carbon dioxide adsorption isotherms of PIA, PIB, PIC, and PID measured at 273 K. (b) Surface areas of PIA, PIB, PIC, and PID measured by nitrogen gas adsorption *vs* their CO_2 capacities measured by CO_2 gas adsorption. (c) Force-field simulation of CO_2 adsorption at 273 K and 1 bar for the four COFs. The figure combines the adsorbed CO_2 density distribution and the potential energy surface, where darker blue areas indicate stronger binding compared to the gray ones.

highest presence of the mesopore sizes observed by PXRD (*i.e.*, the observed crystalline pore size is also the main pore size in gas sorption experiments). While the larger presence of small mesopores over micropores creates an inherent disadvantage for CO_2 capacity, the performances are still comparable with most state-of-the-art microporous COFs. Finally, unlike the other microporous COFs, we expect that the chemical nature of these imide-based COFs provides stable frameworks for CO_2 sorption under industrially realistic (*i.e.*, humid) conditions, which is to be verified in our future research.

2.4. Electrochemical Properties. Each of the four COFs contain active molecules (PMDA or NTCDA), which can undergo redox reactions. The actual redox sites on these organic molecules are at the carbonyl groups. In theory, it is thus possible to reversibly host four alkali metal atoms per active molecule (based on the number of carbonyl groups). This is likely to happen *via* two two-electron transfers, see Figure 8d. However, achieving both transfers requires significantly low discharge potentials and leads to irreversible redox reactions, possibly due to destructive reactions or inactivation of the organic materials. The first two-electron transfer is well known to be (completely) reversible.[13,66−68,71] Hence, the theoretical capacities are calculated based on a two-electron transfer mechanism per active molecule (step 1, Figure 8d).

DFT calculations provide a clear indication that the observed redox reactions correspond to Li and Na binding to the active carbonyl groups of the COF structure. Scanning through the plane of the PID−COF for favorable Li and Na active sites resulted in the energy bonding landscape maps

https://dx.doi.org/10.1021/acs.chemmater.0c03218
Chem. Mater. 2021, 33, 818−833

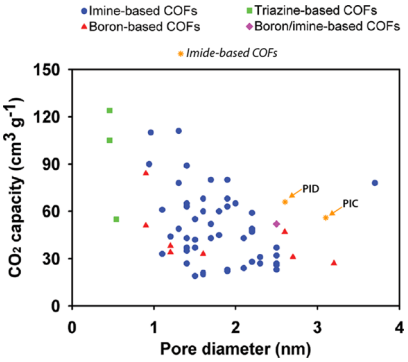

Figure 7. Plot of low-pressure CO_2 uptake against pore diameter for the selected COFs at 273 K and 1 bar. Figure adapted from Zeng *et al.*[57] with the addition of the results presented here. Adapted with permission from ref 57. Copyright 2016, Wiley-VCH.

shown in Figure 8a,b. The most favorable positions (indicated by the dark blue color) are located in the proximity of the oxygen atoms. For both ions, a sharp energy increase is observed as we move away from the carbonyl groups. For Na, the energy landscape is relatively more diffuse, as compared to Li, which strongly prefers to stick near the pore walls. Full relaxation of the most favorable positions for both ions reveals the exact insertion geometry. Li is stabilized at a distance of ~1.8 Å, being shared between two oxygen atoms of adjacent sheets at a calculated redox voltage of ~2.51 V versus Li/Li^+, in good agreement with the experimental results (2.49 V).

Similarly, Na-ions are bonded to the same position at slightly larger distances ~2.1 Å due to their larger ionic radius (Figure 8c). These positions are in line with the expected electrochemical reaction mechanism of polyimides based on PMDA or NTCDA,[13] which is shown in Figure 8d, where ideally four electrons can be transferred in the indicated 2-step scheme. In general, for these materials, step 2 in the redox mechanism results in severe structural damage and irreversible decomposition.[71]

The electrochemical performances of all four COF-materials were determined for lithium- and sodium-ion batteries (LIBs and SIBs) *via* cyclic voltammetry (CV), electrochemical impedance spectroscopy, and galvanostatic cycling (applying a constant current). All COFs are tested in a potential window of 1.5−3.5 V versus Li/Li^+ or Na/Na^+ due to the above reversibility reasons. Each COF, together with a standard electronic conductor (carbon black) and binder (polyvinyl difluoride), was processed in standard non-optimized electrodes and tested as a working electrode against metallic lithium or sodium. The alkali metals acted as the counter and reference electrode. The COF electrodes were not enhanced (*e.g.*, pressed, the addition of nanotubes), and therefore, the electrodes can be considered far from optimized, as the presented focus is the initial evaluation of the electrochemical activity of these materials toward Na (for the aqueous battery).

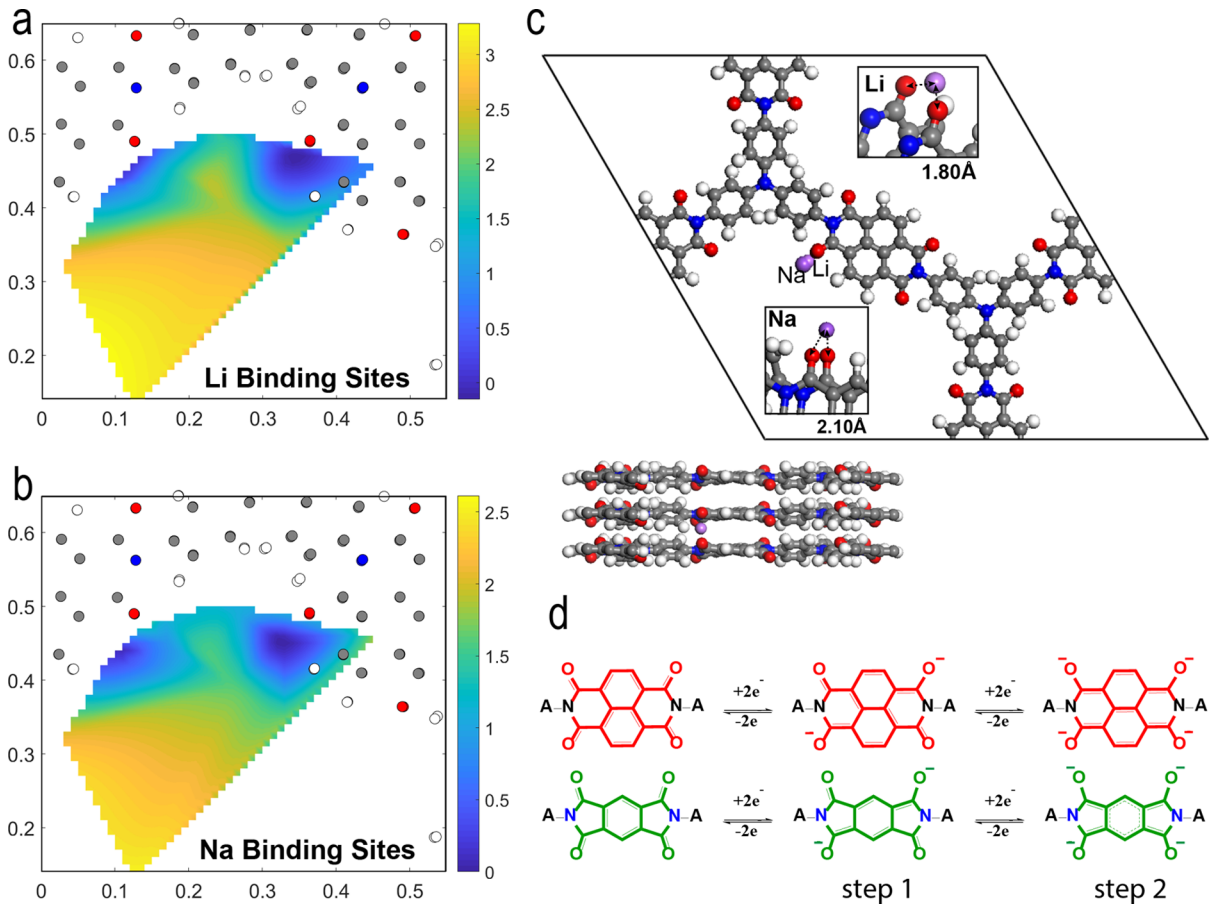

Figure 8. (a) Li and (b) Na insertion in PID *via* DFT calculations; the dark blue areas indicate the most favorable adsorption sites for Li and Na, respectively, and are set as the 0 point reference (scale in eV). (c) Preferable configurational geometry of the intercalated Li and Na. (d) 2-step electron transfer mechanism for the lithiation and sodiation of the COFs.

https://dx.doi.org/10.1021/acs.chemmater.0c03218
Chem. Mater. 2021, 33, 818−833

We want to show the first evidence where imide-based COFs can be used for the sodium aqueous battery, and therefore, we only present our most promising electrochemical results regarding Na insertion, which is for the PID system. The electrochemical results for both Na and Li insertion in the four COFs can be found in the Supporting Information.

The CV of Na insertion in PID shows two clear reversible pairs of oxidation and reduction peaks, see Figure 9a. This

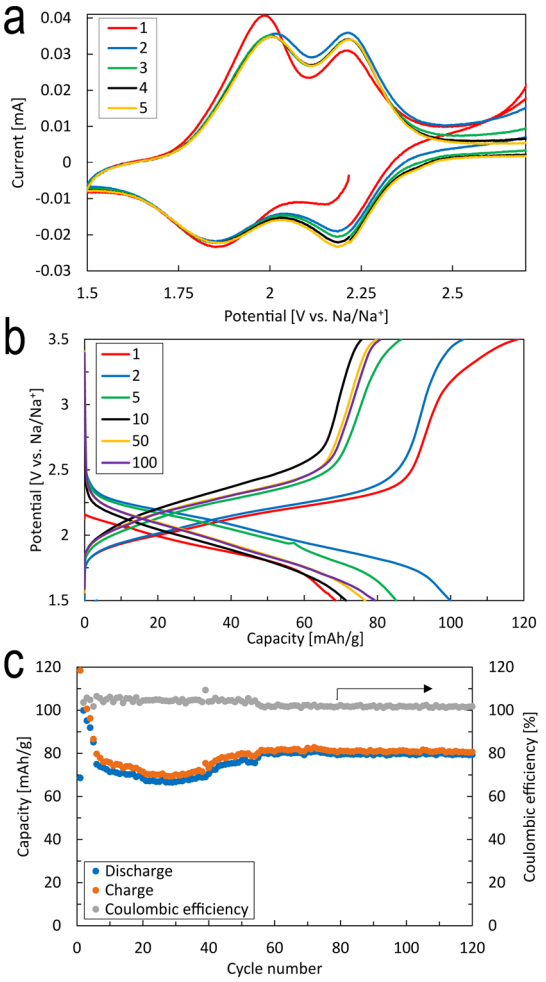

Figure 9. (a) CV curves at a scan rate of 0.1 mV s^{-1}. (b) Charge−discharge profiles and (c) cycling performance at a rate of 0.1 C (15 mA g^{-1}) for PID in SIB.

most likely reflects the sodiation of the first and second carbonyl group, in which the second sodiated group is oppositely located to the first where it experiences the least steric hindrance.[13,69] The presence of two distinct redox pairs has not been observed for other COF electrodes nor for NTCDA electrodes,[13,51,70] which is potentially related to the observed torsion creating more space between adjacent carbonyl groups. Only positive shifts in the potentials of the first reduction (2.16 V *vs* Na/Na^+ to 2.18 V) and oxidation peaks (1.97−2.01 V) differ from the first to the second scan, and the potentials of the other two peaks are not affected. The polarization is small compared to that in the literature.[13,51,69] The complete potential range of the CV of PID in SIB can be found in Figure S31. The large oxidation currents obtained above 2.5 V are irreversible and occur only during the initial five cycles and are induced by the decomposition of the electrolyte, see Figure S32. The presence of the two oxidation and reduction pairs is not noticeable in the charge−discharge profiles, Figure 9b. Only a single sloped potential plateau is observed during cycling, similar to that of the other COF electrodes. There is a substantial potential difference (0.19 V) between the initial and sequential five discharge plateaus. This difference decreases over time. The reversible capacity of PID in the SIBs is much higher and more stable than that in the LIB. A significant loss in capacity (25 mA h g^{-1}) occurs during the initial six cycles, after which it stabilizes, and some capacity is even recovered during long-term cycling. After 130 cycles, it still has a decent capacity of 81 mA h g^{-1} (Figure 9c).

The redox potentials of all COFS, extracted from the CVs, are very comparable with those obtained for PMDA/NTCDA containing diimides in linear polymer electrodes[13] (Table 1).

Table 1. Reduction Potentials of Our NTCDA/PMDA-Based COFs and Linear Polymers from the Literature

material	*vs* Li/Li^+ (V)	*vs* Na/Na^+ (V)
NTCDA (COF) (PIC)	2.51	2.25
NTCDA (COF) (PID)	2.49	2.18
NTCDA (polymer)[13]	2.47	
PMDA (COF) (PIA)	1.93	1.51
PMDA (COF) (PIB)	1.95	1.45
PMDA (polymer)[13]	2.08	

Na insertion occurs at ∼0.27 V below that of the Li-ion insertion, close to the difference of Li/Li^+ and Na/Na^+ standard potentials. This indicates that the larger radius of the Na-ion does not induce a significant additional energy penalty for insertion into COF structures, rationalized by the large COF pores and flexibility. From the four reported COFs in this paper, the most promising material for the application in SIBs appears to be PID, which retains a decent reversible capacity of 81 mA h g^{-1}. Although this capacity stabilizes over more than 100 cycles, it is still significantly lower than its theoretical value (126 mA h g^{-1}). A possible explanation for this is the use of a non-optimized standard electrolyte (1 M $NaClO_4$ in EC/DMC) and non-optimized electrodes.

Electrochemical impedance measurements were performed on the non-optimized electrodes to obtain insights in the kinetics, Figure S33. All the COF electrodes show poor kinetics, where the Nyquist plots indicate large Ohmic resistances, indicating slow charge transfer reactions at the electrode surfaces and poor diffusion of the ions. The poor ion transport may be improved by optimization of the morphology, for instance, as achieved by Gu *et al.*,[54] clearly demonstrating the importance of particle sizes in COF materials. DAAQ−COFs with different stacking thicknesses were prepared ranging from 4−12 up to 100−250 nm particles. The smallest thicknesses outperformed their counterparts by providing more than 4 times the capacity at high rates. Even at low currents, larger capacities are achieved for the smaller particles, indicating the presence of inactive parts due to buried, poorly accessible material for larger COF particles. Another kinetic aspect of primary importance is the electronic conductivity. This is underlined by the work of Luo *et al.*[49] and Wang *et al.*,[72] who improved the electronic conductivity of their COFs by the addition of graphene (PIBN-G) or carbon nanotubes during synthesis. Lower charge-transfer resistance was reported *via* impedance spectroscopy measurements along

https://dx.doi.org/10.1021/acs.chemmater.0c03218
Chem. Mater. 2021, 33, 818−833

with superior rate-capability performance (3 times more capacity at 10 C).[48]

Kim *et al.*[73] investigated the electrochemical properties of the PMDA molecule in macrocycle organic arrangements for Li-ion batteries. This group's results point out that the same active material can experience a wide variety of redox environments depending on the geometry of its arrangement, affecting its electrochemical performance. The poor performance of our PMDA-containing COFs can be attributed to a non-favorable arrangement of the redox unit in the COF arrangement compared to its NTCDA counterpart. It is suggested that the two conjugated rings of NTCDA offer a better electrochemical environment to host the donated electron than the single conjugated ring of PMDA. Regarding the linkage molecules, the TAPA-containing COFs are likely to offer superior pore accessibility, as is discussed in Section 2.2.

The high molecular weight of the electrochemically inactive linkage molecules (TAPA and TAPB) limits the (theoretical) capacities of the investigated COFs instantly to relatively low values: 129, 143, 115, and 126 mA h g^{-1} for PIA, PIB, PIC, and PID, respectively, assuming a two-electron transfer mechanism per active molecule. The obtained capacities are lower than COFs that are able to "store" alkali-ions on their C═N groups and benzene rings at low potentials (≪1.5 V).[50,52,55,74] To increase the specific capacity, future designs of COF-related polyimides should be directed to lighter linkage molecules. For example, usage of 2,4,6-triamino-1,3,5-triazine or 1,3,5-triaminobenzene as the linker instead of TAPA or TAPB. This will raise the theoretical capacities of the PMDA COFs to 199 and 201 mA h g^{-1} and the NTCDA COFs to 168 and 169 mA h g^{-1}.

2.5. Aqueous Performance. Several COFs in organic electrolytes that are reported appear to have an extremely low operation potential (0−1.5 V *vs* Li/Li^+[50,52,55,74] and 0−1 V *vs* Na/Na^+[55,56,75]) and, thus, from this perspective appear to be quite suitable as anode materials for organic electrolyte containing Li-ion and Na-ion batteries. In contrast, the polyimides tested herein have an operating potential above 1.5 V, which seem very suitable for aqueous electrolytes because it is within the stability window of water over a semi wide pH-range. The thermodynamic potential of the hydrogen evolution reaction (HER) at neutral pH is 2.297 versus Na/Na^+, while the practical HER will be even lower due to a substantial polarization of the HER (depending on the electrode materials), suggesting that our NTCDA-containing COFs may be a potential anode material for Na-aqueous batteries. The high abundancy and easier harvest conditions of sodium, as compared to lithium, in combination with an aqueous electrolyte and organic electrodes, make these combinations in potential a cheap, safe, and environmentally friendly battery which is in particular promising for stationary storage applications, where energy density has less priority.[76,77]

Since PID had the best performances in the SIB with organic electrolyte, it was selected to be tested in an aqueous sodium-ion battery. PID was used as the negative electrode and $Na_{0.44}MnO_2$ as the positive electrode in combination with an Ag/AgCl reference electrode. The electrolyte was a 0.5 M Na_2SO_4 aqueous electrolyte with a pH of 7. The CV of PID in the aqueous SIB, Figure 10a, is similar to the one in the organic SIB. Both redox peaks are present during oxidation and reduction, albeit less sharp and have potential shifts of +0.2 to 0.3 V, most likely caused by the different chemical and kinetic environment of the electrolyte. During the galvanostatic

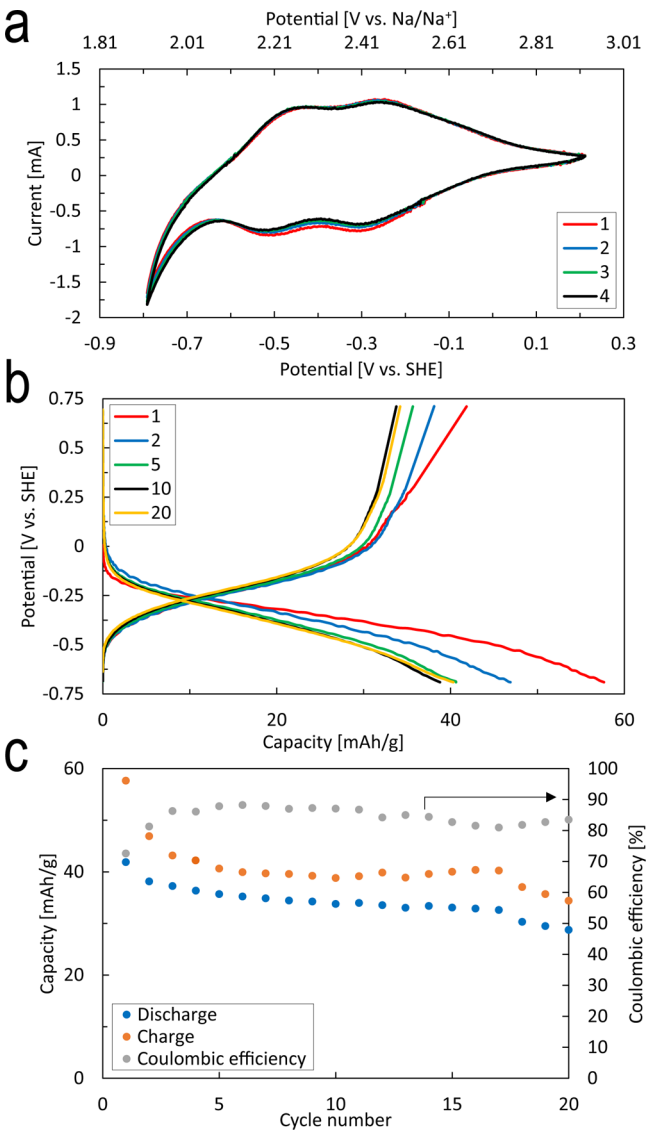

Figure 10. Electrochemical performances of PID in the $Na_{0.44}MnO_2$/PID aqueous sodium-ion battery. (a) CV with a scan rate of 0.1 mV s^{-1}. (b) Charge−discharge profiles of cycle 1, 2, 5, 10, and 20 at a C-rate of 0.1 C (15 mA g^{-1}). (c) Cycling performance at a rate of 0.1 C (16 mA g^{-1}).

cycling test, Figure 10b, the lower cutoff potential of the anode was set at −0.9 V versus Ag/AgCl to be sure to prevent hydrogen evolution. This greatly limits the capacities in these tests, but optimization of the electrolyte (lowering the HER and thus the cutoff) is expected to result in higher capacities. This can be achieved by lowering the pH or by using high Na-salt concentrations,[78,79] but this is out of scope of this paper. The average aqueous operating potential (−0.6 V *vs* Ag/AgCl or 2.31 V *vs* Na/Na^+) is higher (+0.30 to 0.38 V) than that of the average potentials in the organic electrolyte batteries which is consistent with the observed shifts in the CV.

The capacity decreases in the initial five cycles before it stabilizes, see Figure 10c. However, the shape of the voltage profile is identical, indicating reversible Na-ion insertion and extraction from PID. The difference between the charge and discharge capacities can be explained by the fact that the aqueous electrolyte was not purged to get rid of the oxygen. It is well known that dissolved oxygen in the aqueous electrolytes

https://dx.doi.org/10.1021/acs.chemmater.0c03218
Chem. Mater. 2021, 33, 818−833

will react with "bonded" sodium at the anode side, which results in considerable loss in discharge capacities.[66,80,81] Above observed results demonstrate that PID (and probably PIC) can function well as negative electrodes in a Na-aqueous battery. The optimization of the performances is the subject of future studies.

In the same context, Figure 11 and Table 2 present an overview of the COF materials reported in the literature for

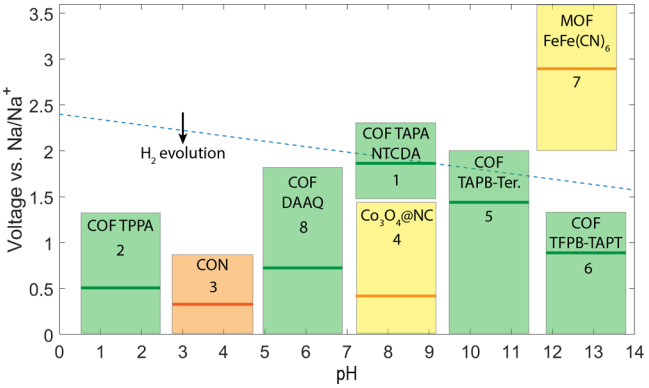

Figure 11. Review of the presented COF material and reported COFs, CON and MOF materials (2−8). The dotted blue line reflects the thermodynamic HER potential as a function of pH. The vertical length of the boxes reflect their tested operational voltage range and the bold line within the boxes correspond to the voltage where half of the reported capacity is reached. The numbering of the boxes refers to the numbers listed in Table 2.

Table 2. Numbers in the First Column Correspond to the Numbering in Figure 11[a]

#	group	system	specific capacity (mA h/g)/current density (mA/g)
1	this work	(COF) TAPA + NTCDA	81/15
2	Zhang *et al.*[55]	(COF) TPPA	238/50 89/2500
3	Kim *et al.*[82]	covalent organic nanosheets	190/200 80/1000
4	Wang *et al.*[83]	Co_3O_4 on nitrogen-doped carbon	506/100 263/1000
5	Zhang and Gao[75]	(COF) TAPB—terephthalaldehyde	303/100 170/1000
6	Patra *et al.*[56]	(COF) TFPB−TAPT	250/30 160/200
7	Nie *et al.*[84]	(MOF) $FeFe(CN)_6$/carbon	82/24
8	Gu *et al.*[54]	(COF) DAAQ	420/100 200/5000

[a]TFPB stands for 1,3,5-tris(4-formyl phenyl) benzene, TAPT stands for 1,3,5-tris(4 amino phenyl)-triazine, and TPPA for triformylphloroglucin-*p*-phenylenediamine.

SIBs along with sister materials such as metal organic frameworks (MOFs) and covalent organic nanosheets (CONs). The potential for sodium insertion into these materials is compared to the theoretical HER potential as a function of pH, indicating the feasibility of these materials in aqueous batteries. In particular, of interest is the work of Zhang and Gao[75] who used the TAPB linkage in combination with the light molecule terephthalaldehyde. Due to its high capacity and the plateau-like region, the material can reach 150 mA h/g at a relatively high voltage and might be relevant for alkaline (pH ≫ 7) aqueous systems; however, stability in water remains to be demonstrated. An interesting direction is to combine the TAPA linkage with terephthalaldehyde which, based on the torsion analysis in Section 2.2, is expected to stabilize the structure even further by allowing a more rotational freedom. The presence of a nitrogen functional group and also in the linkage molecule will further increase the capacity, compared to a benzene counterpart, and is additionally expected to increase the conductivity and wettability of the material.[75]

3. CONCLUSIONS

In summary, we report a synthesis route for producing COFs composed of PMDA or NTCDA with TAPA or TAPB linkage molecules. Computational characterization by DFT reveals the stability and preferred orientation of the molecular components in the COF crystal. The preferential torsion between the benzene rings of the linkage molecules is around 32° introducing longer stacking distances and reducing the pore size compared to their flat (2D) counterparts. Torsion in COF configurations with the TAPA linkage molecule is much more stable due to the presence of the nitrogen atom that allows extra rotational freedom. The stacking of the sheets in the perpendicular direction has AA eclipsed orientations with possible reversible offsets due to metastable phases. These insights guide selecting the right components for advanced nano-architectures for next-generation batteries and other applications.

A brief study on CO_2 uptake of the four COFs was performed and showed clear correlations between CO_2 capacity, surface area, and pore size. In addition, molecular modeling revealed that PIB and PID contain preferred CO_2 binding sites, which emphasized that these COFs were best suited for CO_2 uptake. By combining these computational results with the fact that the best performing COFs (PIB and PID) contain TAPA building blocks, we identified a valuable new structure−property relationship that enables directed research toward novel high-performing CO_2 adsorbents.

Non-optimized NTCDA-related COFs provide reversible capacities tested in LIBs and SIBs. PID in SIBs showed for the first time two clear pairs of redox peaks and also performed the best overall with a capacity of 81 mA h g^{-1} after 130 cycles. The superior performance of the PID (NTCDA−TAPA) compared to that of the PIC (NTCDA−TAPB) material can be attributed to the structural characteristics explored computationally.

The superior stability of the TAPA linkage results in more cohesive particles ensuring the presence of accessible pores. In addition, the longer pore walls might allow ion accessibility in an otherwise inactive pore from the outside. An overview of COFs and similar organic structures evaluated for SIBs brings forward the promises and directions of future material design. The relatively high redox potential of the presented polyimides, combined with the structural stability when utilized in COF configurations, is put in perspective as potential anode materials for aqueous sodium-ion batteries. Usage of COFs in these batteries, in this paper demonstrated with PID, appears to be quite promising. This will open up new directions for the development and utilization of diimide-related configurations as versatile electrode materials in (aqueous) batteries.

https://dx.doi.org/10.1021/acs.chemmater.0c03218
Chem. Mater. 2021, 33, 818−833

4. EXPERIMENTAL SECTION

4.1. General COF Synthesis. A detailed description of the synthesis of the individual polymers is described in the Supporting Information. In general, a 10 mL Pyrex tube was charged with 0.44 mmol of dianhydride monomer (PMDA or NTCDA) and 0.29 mmol of triamine monomer (TAPB or TAPA) in a solution of 1 mL of *m*-cresol/1 mL of NMP in the presence of 0.06 mL of isoquinoline. The tube was degassed *via* three freeze−pump−thaw cycles at 77 K and flame sealed. The tube was then heated at 200 °C for 3 days. The resulting precipitate was washed with methanol (3×) and acetone (3×) and recovered by centrifugation. The resulting compound was purified by Soxhlet extraction in THF for 24 h and then dried at 60 °C under vacuum for 12 h to provide the COF powder.

4.2. Electrode Preparation. Electrodes were fabricated by casting electrode slurries onto current collectors. First, a mixture of one of the active materials (COF or $Na_{0.44}MnO_2$), an electronic conducting agent (Super P, Timcal) and a binder (polyvinylidene fluoride, Solef) in a mass ratio of 8:1:1 was thoroughly ground. NMP (Sigma-Aldrich) was added to the mixture to form a homogeneous viscous slurry. The slurry was cast with a doctor blade on the current collectors, carbon-coated copper foil for organic electrolyte LIBs, and carbon-coated aluminum foil for organic electrolyte SIBs. Carbon-coated foils were used to improve the adhesion of the coating with the current collector. The electrodes for the aqueous SIB were made by casting the slurry on stainless steel. The coatings were dried in a vacuum oven at 80 °C overnight, and circular discs were cut out with an average mass loading of 2.1 mg cm^{-2}.

4.3. Electrochemical Testing. The organic electrolyte LIBs and SIBs were assembled in an Argon-filled glovebox (MBraun). COF-electrodes were placed as working electrodes in self-made Swagelok cells. Lithium or sodium metal discs (Sigma-Aldrich) were used as both counter and reference electrode. Glass fiber discs (Whatman) were used as separators. Standard 1 M $LiPF_6$ (for LIBs) and 1 M $NaClO_4$ (for SIBs) in EC and DMC battery grade solutions (1:1 vol, Sigma-Aldrich) were used as electrolytes. Three electrode cells were used for testing the electrochemical performances of PID as the working electrode in the aqueous sodium-ion battery. $Na_{0.44}MnO_2$ acted as the counter electrode, and an Ag/AgCl electrode (0.197 V *vs* NHE) was used as the reference electrode. A 0.5 M Na_2SO_4 aqueous solution (pH = 7−8) was used as the electrolyte. CV measurements were performed on a potentiostat/galvanostat (PGSTAT302N, Metrohm). CVs were obtained at a scan rate of 0.1 mV s^{-1} with a voltage window of 1.5−3.5 V versus Li/Li^+ or Na/Na^+ for the organic electrolyte batteries and −1.0 to 0 V versus Ag/AgCl for the aqueous battery. Electrochemical cycling of the batteries was conducted on a M4000 Maccor battery tester at a 0.1 C-rate based on the theoretical capacities of the COF-based electrodes.

4.4. Computational Testing. DFT calculations, as implemented in the plane-wave Vienna ab initio simulation package,[85] were performed. The generalized gradient approximation of Perdew−Burke−Ernzerhof[86,87] was selected, while the core-electron interactions were probed with the projector augmented wave method.[88] In order to account for dispersion forces in these large molecules, the zero damping DFT-D3 method of Grimme was implemented. For the geometry optimization of hexagonal unit-cell configurations (AA eclipsed, AB staggered and serrated), a high cutoff energy of 520 eV was selected to ensure accurate calculations. The energy maps are constructed by relaxing configurations with offsets of 0 1.5, 3, 7, 11, and 18.6 Å for the PID and 0, 3, 7, 14, and 21 Å in the direction toward the staggered configurations and configurations with an offset in the respective distances to form hexagons in the diagonal direction (Figure S30). The data points were symmetrically rotated to form the hexagon. Insertion simulations required a 1 × 1 × 3 COF supercell to ensure sufficient Li/Na screening along the tunnel direction. For these relaxations, the cutoff was reduced to 400 eV. The Monkhorst−Pack, *k*-point mesh was set to 3 3 7 and 1 1 3 for the unit and supercell configurations, respectively. In all cases, total energies were obtained from subsequent, self-consistent calculations with a cutoff energy of 520 eV. The simulated PXRD patterns were obtained using the Materials Studio Software package in combination with the Reflex Materials Studio module. The results were based on the DFT-optimized unit cells of the COF materials in several possible configurations. The experimental PXRDs were subjected to Pawley refinement using the pseudo-Voigt peak shape function and Finger−Cox−Jephcoat asymmetry correction function (up to 20°) to produce the refined profile.

■ ASSOCIATED CONTENT

Supporting Information

The Supporting Information is available free of charge at https://pubs.acs.org/doi/10.1021/acs.chemmater.0c03218.

Polymer synthesis procedures, FT-IR spectra, TGAs, stability tests, nitrogen gas sorption measurements, BET-plots, PSDs, solid-state NMR, SEM images, computational methods, crystal structures, CO_2 sequestration, and electrochemistry of organic Li-ion and Na-ion batteries and aqueous Na-ion batteries (PDF)
Crystallographic data for PIA_AA_tor (CIF)
Crystallographic data for PIA_AB_tor (CIF)
Crystallographic data for PIB_AA_tor (CIF)
Crystallographic data for PIB_AB_tor (CIF)
Crystallographic data for PIC_AA_tor (CIF)
Crystallographic data for PIC_AB_tor (CIF)
Crystallographic data for PID_AA_tor (CIF)
Crystallographic data for PID_AB_tor (CIF)
Crystallographic data for PID_SE_tor (CIF)

■ AUTHOR INFORMATION

Corresponding Authors

Marnix Wagemaker − *Storage of Electrochemical Energy, Technische Universiteit Delft, 2629 JB Delft, The Netherlands;* orcid.org/0000-0003-3851-1044; Email: m.wagemaker@tudelft.nl

Atsushi Nagai − *Novel Aerospace Materials, Technische Universiteit Delft, 2629 GB Delft, The Netherlands;* Email: a.nagai@tudelft.nl

Authors

Remco van der Jagt − *Storage of Electrochemical Energy, Technische Universiteit Delft, 2629 JB Delft, The Netherlands;* orcid.org/0000-0003-4239-7758

Alexandros Vasileiadis − *Storage of Electrochemical Energy, Technische Universiteit Delft, 2629 JB Delft, The Netherlands*

Hugo Veldhuizen − *Novel Aerospace Materials, Technische Universiteit Delft, 2629 GB Delft, The Netherlands;* orcid.org/0000-0002-1828-5820

Pengpeng Shao − *School of Chemistry and Chemical Engineering, Beijing Institute of Technology, 100081 Beijing, China*

Xiao Feng − *School of Chemistry and Chemical Engineering, Beijing Institute of Technology, 100081 Beijing, China;* orcid.org/0000-0002-3212-3051

Swapna Ganapathy − *Storage of Electrochemical Energy, Technische Universiteit Delft, 2629 JB Delft, The Netherlands*

Nicolas C. Habisreutinger − *Novel Aerospace Materials, Technische Universiteit Delft, 2629 GB Delft, The Netherlands*

Monique A. van der Veen − *Catalysis Engineering, Technische Universiteit Delft, 2629 HZ Delft, The Netherlands;* orcid.org/0000-0002-0316-4639

Chao Wang − *Storage of Electrochemical Energy, Technische Universiteit Delft, 2629 JB Delft, The Netherlands*

https://dx.doi.org/10.1021/acs.chemmater.0c03218
Chem. Mater. 2021, 33, 818−833

Sybrand van der Zwaag − *Novel Aerospace Materials, Technische Universiteit Delft, 2629 GB Delft, The Netherlands*

Complete contact information is available at: https://pubs.acs.org/10.1021/acs.chemmater.0c03218

Author Contributions

[⊥]R.v.d.J. and A.V. and H.V. contributed equally.

Notes

The authors declare no competing financial interest.

■ ACKNOWLEDGMENTS

The authors thank Kees Goubitz, Michel Steenvoorden, and Frans Ooms (Delft University of Technology, faculty of Applied Sciences) for their assistance with experiments. The authors thank Willy Rook (Delft University of Technology, faculty of Applied Sciences) for her support with gas uptake measurements and interpretation of the data. The authors also thank Dalian University of Technology for the permission to use their Materials Studio software package. Financial support is greatly acknowledged from the Netherlands Organization for Scientific Research (NWO) under the OTP grant no. 15785 and the VICI grant no. 16122.

■ REFERENCES

(1) Schon, T. B.; McAllister, B. T.; Li, P.-F.; Seferos, D. S. The rise of organic electrode materials for energy storage. *Chem. Soc. Rev.* **2016**, *45*, 6405−6406.
(2) Aricò, A. S.; Bruce, P.; Scrosati, B.; Tarascon, J.-M.; Van Schalkwijk, W. Nanostructured materials for advanced energy conversion and storage devices. *Nat. Mater.* **2005**, *4*, 366−377.
(3) Liang, Y.; Tao, Z.; Chen, J. Organic electrode materials for rechargeable lithium batteries. *Adv. Energy Mater.* **2012**, *2*, 742−769.
(4) Song, Z.; Zhou, H. Towards sustainable and versatile energy storage devices: an overview of organic electrode materials. *Energy Environ. Sci.* **2013**, *6*, 2280−2301.
(5) Morita, Y.; Nishida, S.; Murata, T.; Moriguchi, M.; Ueda, A.; Satoh, M.; Arifuku, K.; Sato, K.; Takui, T. Organic tailored batteries materials using stable open-shell molecules with degenerate frontier orbitals. *Nat. Mater.* **2011**, *10*, 947−951.
(6) Wu, H.; Shevlin, S. A.; Meng, Q.; Guo, W.; Meng, Y.; Lu, K.; Wei, Z.; Guo, Z. Flexible and Binder-Free Organic Cathode for High-Performance Lithium-Ion Batteries. *Adv. Mater.* **2014**, *26*, 3338−3343.
(7) Nishide, H.; Oyaizu, K. Toward flexible batteries. *Science* **2008**, *319*, 737−738.
(8) Williams, D. L.; Byrne, J. J.; Driscoll, J. S. A High Energy Density Lithium/Dichloroisocyanuric Acid Battery System. *J. Electrochem. Soc.* **1969**, *116*, 2−4.
(9) Tarascon, J.-M. Key challenges in future Li-battery research. *Philos. Trans. R. Soc., A* **2010**, *368*, 3227−3241.
(10) Palomares, V.; Casas-Cabanas, M.; Castillo-Martínez, E.; Han, M. H.; Rojo, T. Update on Na-based battery materials. A growing research path. *Energy Environ. Sci.* **2013**, *6*, 2312−2337.
(11) Zhong, L.; Lu, Y.; Li, H.; Tao, Z.; Chen, J. High-performance aqueous sodium-ion batteries with hydrogel electrolyte and alloxazine/CMK-3 anode. *ACS Sustainable Chem. Eng.* **2018**, *6*, 7761−7768.
(12) Yang, Y.; Wang, C.; Yue, B.; Gambhir, S.; Too, C. O.; Wallace, G. G. Electrochemically synthesized polypyrrole/graphene composite film for lithium batteries. *Adv. Energy Mater.* **2012**, *2*, 266−272.
(13) Song, Z.; Zhan, H.; Zhou, Y. Polyimides: promising energy-storage materials. *Angew. Chem., Int. Ed.* **2010**, *49*, 8444−8448.
(14) Xie, J.; Zhang, Q. Recent progress in rechargeable lithium batteries with organic materials as promising electrodes. *J. Mater. Chem. A* **2016**, *4*, 7091−7106.
(15) Xu, Y.; Zhou, M.; Lei, Y. Organic materials for rechargeable sodium-ion batteries. *Mater. Today* **2018**, *21*, 60−78.
(16) Cote, A. P.; Benin, A. I.; Ockwig, N. W.; O'Keeffe, M.; Matzger, A. J.; Yaghi, O. M. Porous, crystalline, covalent organic frameworks. *Science* **2005**, *310*, 1166−1170.
(17) El-Kaderi, H. M.; Hunt, J. R.; Mendoza-Cortés, J. L.; Côté, A. P.; Taylor, R. E.; O'Keeffe, M.; Yaghi, O. M. Designed synthesis of 3D covalent organic frameworks. *Science* **2007**, *316*, 268−272.
(18) Feng, X.; Ding, X.; Jiang, D. Covalent organic frameworks. *Chem. Soc. Rev.* **2012**, *41*, 6010−6022.
(19) Hunt, J. R.; Doonan, C. J.; LeVangie, J. D.; Côté, A. P.; Yaghi, O. M. Reticular synthesis of covalent organic borosilicate frameworks. *J. Am. Chem. Soc.* **2008**, *130*, 11872−11873.
(20) Tilford, R. W.; Gemmill, W. R.; zur Loye, H.-C.; Lavigne, J. J. Facile synthesis of a highly crystalline, covalently linked porous boronate network. *Chem. Mater.* **2006**, *18*, 5296−5301.
(21) Spitler, E. L.; Dichtel, W. R. Lewis acid-catalysed formation of two-dimensional phthalocyanine covalent organic frameworks. *Nat. Chem.* **2010**, *2*, 672−677.
(22) Doonan, C. J.; Tranchemontagne, D. J.; Glover, T. G.; Hunt, J. R.; Yaghi, O. M. Exceptional ammonia uptake by a covalent organic framework. *Nat. Chem.* **2010**, *2*, 235−238.
(23) Côté, A. P.; El-Kaderi, H. M.; Furukawa, H.; Hunt, J. R.; Yaghi, O. M. Reticular synthesis of microporous and mesoporous 2D covalent organic frameworks. *J. Am. Chem. Soc.* **2007**, *129*, 12914−12915.
(24) Tilford, R. W.; Mugavero, S. J.; Pellechia, P. J.; Lavigne, J. J. Tailoring microporosity in covalent organic frameworks. *Adv. Mater.* **2008**, *20*, 2741−2746.
(25) Nagai, A.; Guo, Z. Q.; Feng, X.; Jin, S. B.; Chen, X.; Ding, X. P.; Jiang, D. L. Pore surface engineering in covalent organic frameworks. *Nat. Commun.* **2011**, *2*, 536.
(26) Feng, X.; Chen, L.; Dong, Y.; Jiang, D. Porphyrin-based two-dimensional covalent organic frameworks: synchronized synthetic control of macroscopic structures and pore parameters. *Chem. Commun.* **2011**, *47*, 1979−1981.
(27) Chen, X.; Gao, J.; Jiang, D. Designed synthesis of porphyrin-based two-dimensional covalent organic frameworks with highly ordered structures. *Chem. Lett.* **2015**, *44*, 1257−1259.
(28) Bojdys, M. J.; Jeromenok, J.; Thomas, A.; Antonietti, M. Rational extension of the family of layered, covalent, triazine-based frameworks with regular porosity. *Adv. Mater.* **2010**, *22*, 2202−2205.
(29) Spitler, E. L.; Koo, B. T.; Novotney, J. L.; Colson, J. W.; Uribe-Romo, F. J.; Gutierrez, G. D.; Clancy, P.; Dichtel, W. R. A 2D covalent organic framework with 4.7-nm pores and insight into its interlayer stacking. *J. Am. Chem. Soc.* **2011**, *133*, 19416−19421.
(30) Wan, S.; Gándara, F.; Asano, A.; Furukawa, H.; Saeki, A.; Dey, S. K.; Liao, L.; Ambrogio, M. W.; Botros, Y. Y.; Duan, X.; Seki, S.; Stoddart, J. F.; Yaghi, O. M. Covalent organic frameworks with high charge carrier mobility. *Chem. Mater.* **2011**, *23*, 4094−4097.
(31) Wan, S.; Guo, J.; Kim, J.; Ihee, H.; Jiang, D. A belt-shaped, blue luminescent, and semiconducting covalent organic framework. *Angew. Chem., Int. Ed.* **2008**, *47*, 8826−8830.
(32) Wan, S.; Guo, J.; Kim, J.; Ihee, H.; Jiang, D. A photoconductive covalent organic framework: self-condensed arene cubes composed of eclipsed 2D polypyrene sheets for photocurrent generation. *Angew. Chem., Int. Ed.* **2009**, *48*, 5439−5442.
(33) Ding, X.; Guo, J.; Feng, X.; Honsho, Y.; Guo, J.; Seki, S.; Maitarad, P.; Saeki, A.; Nagase, S.; Jiang, D. Synthesis of metallophthalocyanine covalent organic frameworks that exhibit high carrier mobility and photoconductivity. *Angew. Chem., Int. Ed.* **2011**, *50*, 1289−1293.
(34) Ding, X.; Chen, L.; Honsho, Y.; Feng, X.; Saengsawang, O.; Guo, J.; Saeki, A.; Seki, S.; Irle, S.; Nagase, S.; Parasuk, V.; Jiang, D. An n-Channel Two-Dimensional Covalent Organic Framework. *J. Am. Chem. Soc.* **2011**, *133*, 14510−14513.
(35) Feng, X.; Liu, L.; Honsho, Y.; Saeki, A.; Seki, S.; Irle, S.; Dong, Y.; Nagai, A.; Jiang, D. High-Rate Charge-Carrier Transport in Porphyrin Covalent Organic Frameworks: Switching from Hole to

Electron to Ambipolar Conduction. *Angew. Chem., Int. Ed.* **2012**, *51*, 2618−2622.
(36) Feng, X.; Chen, L.; Honsho, Y.; Saengsawang, O.; Liu, L.; Wang, L.; Saeki, A.; Irle, S.; Seki, S.; Dong, Y.; Jiang, D. An Ambipolar Conducting Covalent Organic Framework with Self-Sorted and Periodic Electron Donor-Acceptor Ordering. *Adv. Mater.* **2012**, *24*, 3026−3031.
(37) Patwardhan, S.; Kocherzhenko, A. A.; Grozema, F. C.; Siebbeles, L. D. A. Delocalization and mobility of charge carriers in covalent organic frameworks. *J. Phys. Chem. C* **2011**, *115*, 11768−11772.
(38) Lanni, L. M.; Tilford, R. W.; Bharathy, M.; Lavigne, J. J. Enhanced hydrolytic stability of self-assembling alkylated two-dimensional covalent organic frameworks. *J. Am. Chem. Soc.* **2011**, *133*, 13975−13983.
(39) Campbell, N. L.; Clowes, R.; Ritchie, L. K.; Cooper, A. I. Rapid microwave synthesis and purification of porous covalent organic frameworks. *Chem. Mater.* **2009**, *21*, 204−206.
(40) Kandambeth, S.; Venkatesh, V.; Shinde, D. B.; Kumari, S.; Halder, A.; Verma, S.; Banerjee, R. Self-templated chemically stable hollow spherical covalent organic framework. *Nat. Commun.* **2015**, *6*, 6786.
(41) Lin, L.-C.; Choi, J.; Grossman, J. C. Two-dimensional covalent triazine framework as an ultrathin-film nanoporous membrane for desalination. *Chem. Commun.* **2015**, *51*, 14921−14924.
(42) Uribe-Romo, F. J.; Doonan, C. J.; Furukawa, H.; Oisaki, K.; Yaghi, O. M. Crystalline covalent organic frameworks with hydrazone linkages. *J. Am. Chem. Soc.* **2011**, *133*, 11478−11481.
(43) Dalapati, S.; Jin, S.; Gao, J.; Xu, Y.; Nagai, A.; Jiang, D. An azine-linked covalent organic framework. *J. Am. Chem. Soc.* **2013**, *135*, 17310−17313.
(44) Nagai, A.; Chen, X.; Feng, X.; Ding, X.; Guo, Z.; Jiang, D. A Squaraine-Linked Mesoporous Covalent Organic Framework. *Angew. Chem., Int. Ed.* **2013**, *52*, 3770−3774.
(45) Fang, Q.; Zhuang, Z. B.; Gu, S.; Kaspar, R. B.; Zheng, J.; Wang, J. H.; Qiu, S. L.; Yan, Y. S. Designed synthesis of large-pore crystalline polyimide covalent organic frameworks. *Nat. Commun.* **2014**, *5*, 4503.
(46) Johnston, J. C.; Meador, M. A. B.; Alston, W. B. A mechanistic study of polyimide formation from diester-diacids. *J. Polym. Sci., Part A: Polym. Chem.* **1987**, *25*, 2175−2183.
(47) Jiang, L.; Tian, Y.; Sun, T.; Zhu, Y.; Ren, H.; Zou, X.; Ma, Y.; Meihaus, K. R.; Long, J. R.; Zhu, G. A crystalline polyimide porous organic framework for selective adsorption of acetylene over ethylene. *J. Am. Chem. Soc.* **2018**, *140*, 15724−15730.
(48) Veldhuizen, H.; Vasileiadis, A.; Wagemaker, M.; Mahon, T.; Mainali, D. P.; Zong, L.; Zwaag, S.; Nagai, A. Synthesis, characterization, and CO_2 uptake of mellitic triimide-based covalent organic frameworks. *J. Polym. Sci., Part A: Polym. Chem.* **2019**, *57*, 2373−2377.
(49) Luo, Z.; Liu, L.; Ning, J.; Lei, K.; Lu, Y.; Li, F.; Chen, J. A microporous covalent−organic framework with abundant accessible carbonyl groups for lithium-ion batteries. *Angew. Chem., Int. Ed.* **2018**, *57*, 9443−9446.
(50) Yang, H.; Zhang, S.; Han, L.; Zhang, Z.; Xue, Z.; Gao, J.; Li, Y.; Huang, C.; Yi, Y.; Liu, H.; Li, Y. High conductive two-dimensional covalent organic framework for lithium storage with large capacity. *ACS Appl. Mater. Interfaces* **2016**, *8*, 5366−5375.
(51) Yang, D.-H.; Yao, Z.-Q.; Wu, D.; Zhang, Y.-H.; Zhou, Z.; Bu, X.-H. Structure-modulated crystalline covalent organic frameworks as high-rate cathodes for Li-ion batteries. *J. Mater. Chem. A* **2016**, *4*, 18621−18627.
(52) Bai, L.; Gao, Q.; Zhao, Y. Two fully conjugated covalent organic frameworks as anode materials for lithium ion batteries. *J. Mater. Chem. A* **2016**, *4*, 14106−14110.
(53) Wang, S.; Wang, Q.; Shao, P.; Han, Y.; Gao, X.; Ma, L.; Yuan, S.; Ma, X.; Zhou, J.; Feng, X.; Wang, B. Exfoliation of covalent organic frameworks into few-layer redox-active nanosheets as cathode materials for lithium-ion batteries. *J. Am. Chem. Soc.* **2017**, *139*, 4258−4261.
(54) Gu, S.; Wu, S.; Cao, L.; Li, M.; Qin, N.; Zhu, J.; Wang, Z.; Li, Y.; Li, Z.; Chen, J.; Lu, Z. Tunable redox chemistry and stability of radical intermediates in 2D covalent organic frameworks for high performance sodium ion batteries. *J. Am. Chem. Soc.* **2019**, *141*, 9623−9628.
(55) Zhang, X.; Zhu, G.; Wang, M.; Li, J. B.; Lu, T.; Pan, L. K. Covalent-organic-frameworks derived N-doped porous carbon materials as anode for superior long-life cycling lithium and sodium ion batteries. *Carbon* **2007**, *116*, 686−694.
(56) Patra, B. C.; Das, S. K.; Ghosh, A.; Raj K, A.; Moitra, P.; Addicoat, M.; Mitra, S.; Bhaumik, A.; Bhattacharya, S.; Pradhan, A. Covalent organic framework based microspheres as an anode material for rechargeable sodium batteries. *J. Mater. Chem. A* **2018**, *6*, 16655−16663.
(57) Zeng, Y.; Zou, R.; Zhao, Y. Covalent Organic Frameworks for CO_2 capture. *Adv. Mater.* **2016**, *28*, 2855−2873.
(58) Dawson, R.; Stöckel, E.; Holst, J. R.; Adams, D. J.; Cooper, A. I. Microporous organic polymers for carbon dioxide capture. *Energy Environ. Sci.* **2011**, *4*, 4239−4245.
(59) Huang, N.; Chen, X.; Krishna, R.; Jiang, D. Two−Dimensional Covalent Organic Frameworks for Carbon Dioxide Capture through Channel−Wall Functionalization. *Angew. Chem.* **2015**, *127*, 3029−3033.
(60) Lee, G.-Y.; Lee, J.; Vo, H. T.; Kim, S.; Lee, H.; Park, T. Amine−Functionalized Covalent Organic Framework for Efficient SO_2 Capture with High Reversibility. *Sci. Rep.* **2017**, *7*, 557.
(61) Wu, S.; Gu, S.; Zhang, A.; Yu, G.; Wang, Z.; Jian, J.; Pan, C. A rational construction of microporous imide−bridged covalent−organic polytriazines for high−enthalpy small gas absorption. *J. Mater. Chem. A* **2015**, *3*, 878−885.
(62) Ma, T.; Kapustin, E. A.; Yin, S. X.; Liang, L.; Zhou, Z.; Niu, J.; Li, L.-H.; Wang, Y.; Su, J.; Li, J.; Wang, X.; Wang, W. D.; Wang, W.; Sun, J.; Yaghi, O. M. Single-crystal x-ray diffraction structures of covalent organic frameworks. *Science* **2018**, *361*, 48−52.
(63) Klimeš, J.; Bowler, D. R.; Michaelides, A. Van der Waals density functionals applied to solids. *Phys. Rev. B: Condens. Matter Mater. Phys.* **2011**, *83*, 195131.
(64) Dion, M.; Rydberg, H.; Schroder, E.; Langreth, D. C.; Lundqvist, B. I. Van der Waals density functional for general geometries. *Phys. Rev. Lett.* **2004**, *92*, 246401.
(65) Nazarian, D.; Ganesh, P.; Sholl, D. S. Benchmarking density functional theory predictions of framework structures and properties in a chemically diverse test set of metal−organic frameworks. *J. Mater. Chem. A* **2015**, *3*, 22432−22440.
(66) Deng, W.; Shen, Y.; Qian, J.; Yang, H. A polyimide anode with high capacity and superior cyclability for aqueous Na-ion batteries. *Chem. Commun.* **2015**, *51*, 5097−5099.
(67) Han, X.; Chang, C.; Yuan, L.; Sun, T.; Sun, J. Aromatic carbonyl derivative polymers as high-performance Li-ion storage materials. *Adv. Mater.* **2007**, *19*, 1616−1621.
(68) Tian, D.; Zhang, H.-Z.; Zhang, D.-S.; Chang, Z.; Han, J.; Gao, X.-P.; Bu, X.-H. Li-ion storage and gas adsorption properties of porous polyimides (PIs). *RSC Adv.* **2014**, *4*, 7506−7510.
(69) Banda, H.; Damien, D.; Nagarajan, K.; Hariharan, M.; Shaijumon, M. M. A polyimide based all-organic sodium ion battery. *J. Mater. Chem. A* **2015**, *3*, 10453−10458.
(70) Xu, F.; Jin, S. B.; Zhong, H.; Wu, D. C.; Yang, X. Q.; Chen, X.; Wei, H.; Fu, R.; Jiang, D. L. Electrochemically active, crystalline, mesoporous covalent organic frameworks on carbon nanotubes for synergistic lithium-ion battery energy storage. *Sci. Rep.* **2015**, *5*, 8225.
(71) Shi, Y.; Tang, H.; Jiang, S.; Kayser, L. V.; Li, M.; Liu, F.; Ji, F.; Lipomi, D. J.; Ong, S. P.; Chen, Z. Understanding the electrochemical properties of naphthalene diimide: implication for stable and high-rate lithium-ion battery electrodes. *Chem. Mater.* **2018**, *30*, 3508−3517.
(72) Wang, G.; Chandrasekhar, N.; Biswal, B. P.; Becker, D.; Paasch, S.; Brunner, E.; Addicoat, M.; Yu, M.; Berger, R.; Feng, X. A crystalline, 2D polyarylimide cathode for ultrastable and ultrafast Li storage. *Adv. Mater.* **2019**, *31*, 1901478.

(73) Kim, D. J.; Hermann, K. R.; Prokofjevs, A.; Otley, M. T.; Pezzato, C.; Owczarek, M.; Stoddart, J. F. Redox-active macrocycles for organic rechargeable batteries. *J. Am. Chem. Soc.* **2017**, *139*, 6635−6643.
(74) Lei, Z.; Yang, Q. S.; Xu, Y.; Guo, S. Y.; Sun, W. W.; Liu, H.; Lv, L. P.; Zhang, Y.; Wang, Y. Boosting lithium storage in covalent organic framework via activation of 14-electron redox chemistry. *Nat. Commun.* **2018**, *9*, 576.
(75) Zhang, Y.; Gao, Z. High performance anode material for sodium-ion batteries derived from covalent-organic frameworks. *Electrochim. Acta* **2019**, *301*, 23−28.
(76) Posada, J. O. G.; Rennie, A. J. R.; Villar, S. P.; Martins, V. L.; Marinaccio, J.; Barnes, A.; Glover, C. F.; Worsley, D. A.; Hall, P. J. Aqueous batteries as grid scale energy storage solutions. *Renewable Sustainable Energy Rev.* **2017**, *68*, 1174−1182.
(77) Kim, H.; Hong, J.; Park, K.-Y.; Kim, H.; Kim, S.-W.; Kang, K. Aqueous rechargeable Li and Na ion batteries. *Chem. Rev.* **2014**, *114*, 11788−11827.
(78) Suo, L.; Borodin, O.; Wang, Y.; Rong, X.; Sun, W.; Fan, X.; Xu, S.; Schroeder, M. A.; Cresce, A. V.; Wang, F.; Yang, C.; Hu, Y.-S.; Xu, K.; Wang, C. "Water-in-salt" electrolyte makes aqueous sodium-ion battery safe, green, and long-lasting. *Adv. Energy Mater.* **2017**, *7*, 1701189.
(79) Kühnel, R.-S.; Reber, D.; Battaglia, C. A high-voltage aqueous electrolyte for sodium-ion batteries. *ACS Energy Lett.* **2017**, *2*, 2005−2006.
(80) Luo, J.-Y.; Cui, W.-J.; He, P.; Xia, Y.-Y. Raising the cycling stability of aqueous lithium-ion batteries by eliminating oxygen in the electrolyte. *Nat. Chem.* **2010**, *2*, 760−765.
(81) Wu, X.; Cao, Y.; Ai, X.; Qian, J.; Yang, H. A low-cost and environmentally benign aqueous rechargeable sodium-ion battery based on $NaTi_2(PO_4)_3$−$Na_2NiFe(CN)_6$ intercalation chemistry. *Electrochem. Commun.* **2013**, *31*, 145−148.
(82) Kim, M.-S.; Lee, W.-J.; Paek, S.-M.; Park, J. K. Covalent organic nanosheets as effective sodium-ion storage materials. *ACS Appl. Mater. Interfaces* **2018**, *10*, 32102−32111.
(83) Wang, Y.; Wang, C.; Wang, Y.; Liu, H.; Huang, Z. Superior sodium-ion storage performance of Co_3O_4@nitrogen-doped carbon: derived from a metal−organic framework. *J. Mater. Chem. A* **2016**, *4*, 5428−5435.
(84) Nie, P.; Shen, L.; Pang, G.; Zhu, Y.; Xu, G.; Qing, Y.; Dou, H.; Zhang, X. Flexible metal−organic frameworks as superior cathodes for rechargeable sodium-ion batteries. *J. Mater. Chem. A* **2015**, *3*, 16590−16597.
(85) Kresse, G.; Furthmüller, J. Efficiency of ab-initio total energy calculations for metals and semiconductors using a plane-wave basis set. *Comput. Mater. Sci.* **1996**, *6*, 15−50.
(86) Perdew, J. P.; Burke, K.; Ernzerhof, M. Generalized gradient approximation made simple. *Phys. Rev. Lett.* **1996**, *77*, 3865−3868.
(87) Lee, B.-J.; Shim, J. H.; Baskes, M. I. Semiempirical atomic potentials for the fcc metals Cu, Ag, Au, Ni, Pd, Pt, Al, and Pb based on first and second nearest-neighbor modified embedded atom method. *Phys. Rev. B: Condens. Matter Mater. Phys.* **2003**, *68*, 144112.
(88) Blöchl, P. E. Projector augmented-wave method. *Phys. Rev. B: Condens. Matter Mater. Phys.* **1994**, *50*, 17953−17979.

https://dx.doi.org/10.1021/acs.chemmater.0c03218
Chem. Mater. 2021, 33, 818−833